Optical Recombination of the LIGO 40-m Gravitational Wave Interferometer

T.T. Lyons,[*] A. Kuhnert,[†] F.J. Raab, J.E. Logan,[†] D. Durance, R.E. Spero,[†] S. Whitcomb, B. Kells
LIGO Project, California Institute of Technology, Pasadena, California 91125

I Introduction

The goal of the LIGO (Laser Interferometer Gravitational-wave Observatory) project is to make the first direct detection of gravitational waves and to use these waves to learn about violent events in the distant universe.[1] The LIGO project is currently building two 4 km long laser interferometer gravitational-wave detectors, one near Hanford, Washington, and the other near Livingston, Louisiana. Full-scale interferometric gravitational wave detectors are also currently under construction by the VIRGO[2] and GEO600[3] projects in Europe. These detectors will be sensitive to relative displacements of their test masses of $10^{-21}\ \mathrm{m}/\sqrt{\mathrm{Hz}}$ in the frequency band from approximately 10 Hz to several 1000 Hz.

LIGO operates a 40 m long interferometer on the campus of the California Institute of Technology, which is used in studying the noise sources limiting interferometric detectors and as a prototype for the larger interferometers under construction. Laser interferometer gravitational wave detectors have many noise sources which could limit their ultimate sensitivity. The three fundamental noise sources which we believe will limit the LIGO detectors are seismic noise, thermal noise and photon shot noise, as shown in Figure 1. In practice our experience with the 40-m intereferometer has shown that other noise sources due to mechanical, optical, or electrical imperfections often limit the sensitivity over some part of the frequency band. One of the challenges of the 40-m interferometer research program is to gain the experience necessary to assure that LIGO will not be limited by these technical noise sources.

Photon shot noise is expected to be the dominant noise source for LIGO at frequencies above approximately 300 Hz. The sensitivity limit imposed by photon shot noise depends on the optical configuration of the interferometer as well as the technique employed to read out the relative positions of the test masses. There has been considerable effort devoted to exploring novel optical configurations and readout schemes that improve the shot noise limited performance of the detectors without requiring unreasonably high power levels in the interferometer.

An obvious candidate for measuring the transverse shear strain produced by a gravitational wave is a Michelson interferometer and in fact early detectors used this configuration.[4,5,6] The antisymmetric port is held on a dark fringe.[‡] A passing gravitational wave from directly overhead

---

[*] Present address, Mission Research Corporation, 3625 Del Amo Boulevard, Suite 215, Torrance, California 90503.

[†] Present address, Jet Propulsion Laboratory, 4800 Oak Grove Drive, Pasadena, California 91109.

will cause the length of one arm of the interferometer to decrease and the other to increase, thus disturbing the dark fringe at the antisymmetric port and providing a signal.

The sensitivity of the Michelson interferometer can be improved by having the light make several round trips in each arm by inserting another mirror between the beam splitter and the end-mirror. The most conceptually simple way to do this is using an optical delay line, where the light strikes the mirrors in a different spot on each round trip. This method will be used in arms of the GEO 600 effort to detect gravitational waves. Another way to do this is to have the light return back to the same spot on both mirrors and form a Fabry-Perot resonant cavity.[7] Such a cavity is said to be resonant when the light entering through the partially transmitting front mirror interferes constructively with the light travelling back and forth inside it. Near resonance the phase of the light returning from the cavity is very sensitive to the deviation from resonance. Thus the effect of a small displacement on the antisymmetric port dark fringe is amplified.

The shot noise limited sensitivity can be improved by increasing the amount of power incident on the beam splitter. Because the light returning from the two arms interferes destructively at the antisymmetric port, the light returning towards the laser must interfere constructively. By inserting a partially transmitting “recycling mirror” between the beam splitter and the laser, this power may be redirected into the interferometer and reused. Of course the recycling mirror must be positioned so that light it reflects back into the interferometer interferes constructively with the light transmitted through it from the laser. This technique, which increases the effective laser power, is known as power recycling.[8]

The initial interferometer design chosen for LIGO is an asymmetric power recycled Michelson with Fabry-Perot arm cavities, as shown in Figure 2, hereafter referred to simply as a recycled interferometer. Four degrees of freedom need to be controlled, as shown in Figure 3. These are the recycling cavity length $(l_1 + l_2)$, the Michelson near-mirror difference $(l_1 - l_2)$, the common mode arm cavity length $(L_1 + L_2)$, and the arm cavity length difference $(L_1 - L_2)$ which gives the gravitational wave signal. Two schemes for extracting signals proportional to these degrees of freedom have been evaluated.[9,10]

Since its original commissioning, until April 5, 1995, the 40-m interferometer was operated as a Fabry-Perot interferometer as shown in Figure 4.[*] In this configuration the light returning from the two arms was independently sensed by two photodiodes. As a result of the calculations described below, the decision was made to proceed in steps towards the goal of a recycled interferometer. The modification of the 40-m interferometer to a recombined optical topology using the asymmetry signal extraction scheme as shown in Figure 5 was the first step and is the focus of this paper. This is the first time that a control scheme that is easily extensible to a power recycled interferometer has been implemented in a suspended interferometer.[11] Since this work was completed, a recycled optical topology has been implemented in the 40-m interferometer.

[‡] The side of the beam splitter facing towards the laser is called the symmetric port because, for equal arm lengths, the light at this port interferes constructively and carries a signal proportional to the average of the arm lengths, while the light at the antisymmetric port interferes destructively and carries a signal proportional to the difference of the arm lengths.

[*] In this figure the demodulation phase is modulo 2π with respect to 0° demodulation defined by the phase of the sidebands as they are incident on the vertex test masses. The phases can be different for the two arms in general. In practice these phases are adjusted empirically to maximize the desired signal.

The start of this work marked an important turning point for the research program of the 40-m interferometer. Previous work had concentrated almost entirely on improving the displacement sensitivity of the interferometer, primarily by understanding and reducing technical noise sources. By late 1994 it was believed that, except for the frequency band from 100-300 Hz, the 40-m interferometer sensitivity was limited only by the three fundamental noise sources expected for LIGO and that the scaling of these noise sources to LIGO sizes was understood. (See Figure 6.) At this point a decision was reached to move from improving the displacement sensitivity to demonstrating the technology needed for LIGO before the final design for the various LIGO subsystems was frozen. The first step in this demonstration was the length sensing and control scheme.

The original plan adopted was to include both signal extraction schemes for sensing the auxiliary degrees of freedom* in the initial LIGO detectors.[12] This decision was reached because of concerns about lock acquisition using the asymmetry signal extraction scheme. Partially as a result of this work and its success in acquiring lock as described in Section III, the decision has been made to only implement the asymmetry signal extraction scheme in the initial LIGO.

II Theory

A diagram of the recombined optical topology with asymmetry scheme signal extraction is shown in Figure 7.† The beam splitter and arm cavity mirrors are labelled as mirrors 2 through 6.‡ For a non-recycled interferometer, the $l_1 + l_2$ degree of freedom is not important. The asymmetry is the DC value of $l_1 - l_2$.** The three extracted signals are v_1, v_2, and v_3. The signal v_1 is used to control the common mode arm cavity length and is fed back to the laser frequency servo. The signal v_2 is fed back to control the beam splitter position. The signal v_3 is used to control the differential arm cavity length. All three signals depend primarily on the degree of freedom they control, but also have some dependence on the other degrees of freedom.

Interferometer Parameters

The parameters used in the calculations discussed below are shown in Table 1. The losses quoted are representative of what is typically seen from in-situ measurements in the 40-m interferometer and are assumed to be split evenly between the mirrors.†† Both arms appear to have a much higher loss than what was expected from measurements of individual test masses before installation in the 40-m interferometer.

---

* Auxiliary degrees of freedom are all degrees of freedom except for the arm cavity length difference which provides the gravitational wave signal.

† In this figure the demodulation phase is modulo 2π with respect to 0° demodulation defined by the phase of the sidebands as they are incident on the beam splitter. In practice the demodulation phases are adjusted empirically.

‡ This convention is to maintain the same numbering scheme as papers on recycling where the recycling mirror would be mirror 1.

** In a non-recycled interferometer these lengths are defined relative to the beam splitter instead of the recycling mirror.

†† For a high finesse Fabry-Perot cavity it is not important where the losses are distributed.

The arm cavity input couplers have regions of increased transmission by 4 - 9 ppm in their centers with FWHM of 5 mm.[*] The transmission values given are measured from in-situ measurements of the degree of overcoupling of the cavities.[13] These values are 20 ppm higher for both input mirrors than the transmissions measured in the optics lab before installation in the 40-m interferometer. This is likely due to a chemical cleaning process the test masses were subjected to before being installed, but after the optics lab measurements were taken.[†] This may also explain some of the increased losses. This process was tried as an alternative to drag wiping and as a potential method which could be used in-situ.

The asymmetry used was the maximum that could reasonably be accommodated in the 40-m interferometer vacuum system. The modulation frequency was selected to be high enough so that the argon-ion laser's intensity noise was shot noise limited, to be away from other RF sources,[‡] and to be a frequency for which a crystal reference can easily be purchased. The modulation index is selected for best performance acquiring lock as is discussed in Section III.

For a laser interferometer with Fabry-Perot arms, the definition of contrast is somewhat ambiguous. The definition we shall use here is:

$$C \equiv \frac{P_B - P_D}{P_B + P_D} \qquad (1)$$

where P_B and P_D are the maximum and minimum power in the carrier light measured at the antisymmetric port. P_B will be measured when both arm cavities are off resonance and there is constructive interference at the antisymmetric port,[**] while P_D will be measured when both arm cavities are on resonance and there is destructive interference at the antisymmetric port.

Matrix of Discriminants

For a recombined interferometer there are three degrees of freedom which need to be controlled. It is useful to consider the deviation of these three degrees of freedom from their optimal operating point both in units of meters and round-trip phase at the laser frequency. We denote these distances by,

---

[*] This defect is an artifact of the coating process.

[†] The chemical cleaning process is known as SC1 in the electronics industry. It removes organics and group IB and IIB metals through reactions of H_2O_2, NH_4OH, and deionized H_2O. The process was to soak the optic in an ultrasonic bath of acetone for 5 minutes. The optic was next soaked in an ultrasonic bath of methanol for 5 minutes. Then the optic was immersed in a solution of H_2O_2 : NH4OH : H_2O (deionized) in a ratio of 1:1:5 at 80°C for 5 minutes. Finally the optic was rinsed in 18 MΩ deionized water. This process was originally developed to clean the surface of silicon wafers before coating them and etches away the surface layers of the material. It is likely that the resulting change in the thickness of the topmost silicon dioxide layer of the mirror coating was responsible for the transmission change.

[‡] Radio stations are the typical source of concern.

[**] Effectively, P_B equals the incident power. One could also define P_B to be measured with the arm cavities held on resonance. In this case P_B would equal the incident power times the arm cavity visibility.

$$\Delta_+ = L_1 + L_2 - \Delta_+^{DC} \quad \delta_- = l_1 - l_2 - \delta_-^{DC} \quad \Delta_- = L_1 - L_2 - \Delta_-^{DC} \tag{2}$$

where Δ_+^{DC} and Δ_-^{DC} are the optimal static common and differential mode lengths and δ_-^{DC} is the optimal static Michelson near mirror difference (asymmetry). The nominal value of δ_-^{DC} is δ.

The three degrees of freedom in units of round trip phase, ignoring the Guoy phase,* at the laser frequency are,

$$\Phi_+ = \frac{4\pi}{\lambda}\Delta_+ \quad \phi_- = \frac{4\pi}{\lambda}\delta_- \quad \Phi_- = \frac{4\pi}{\lambda}\Delta_- \tag{3}$$

The optimal operating point for these degrees of freedom are that they equal zero, modulo 2π.

We can extract signals proportional to the three degrees of freedom by demodulating the light returning towards the laser at the symmetric port and the light emerging from the antisymmetric port. The light at the symmetric port we demodulate with two different phases to give us two independent signals. Each of these signals is largely dependent only on one degree of freedom. The matrix which specifies the change in a particular signal induced by a change in a degree of freedom is the matrix of discriminants. It gives the relative sensitivity each extracted signal has to the three degrees of freedom that need to be controlled.

The matrix of discriminants was calculated using a numerical model, originally developed by M. Regehr.[9] No approximations are made other than that of only considering the carrier, first and second order sidebands. The relative sensitivities of the signals to changes in the three degrees of freedom calculated with the numerical model is shown in Table 2, normalized so that the gravitational wave readout sensitivity is one.† Thus for example,

$$\frac{\partial v_1}{\partial \Phi_+} = -7.8 \tag{4}$$

Notice that the sensitivity to arm cavity common mode motion is higher than the sensitivity to differential motion. This is because the small 50-cm asymmetry provides poor transmission of the RF sidebands to the antisymmetric port and good transmission to the symmetric port.‡ The off-diagonal terms arise predominantly because of the unbalanced beam splitter and arm cavity reflectivities. These break the symmetry of the interferometer and cause mixing of the common and differential mode signals.

---

* The Guoy phase is the phase deficit due to the finite transverse size of the laser beam. The arm cavities were designed to utilize the Guoy phase’s discrimination between spatial modes. If the TEM_{00} mode is resonant, the only other modes to match the resonance condition in the cavity are very high order. In the calculations that follow we shall ignore the Guoy phase as it has a much smaller dependence on z than the propagation phase.

† The matrix of discriminants calculated here were verified independently by R. Weiss using a different numerical model.

‡ This is improved in the recycled configuration.

Shot Noise

As derived in reference 14, the differential mode displacement equivalent to shot noise in the gravitational wave readout is given by:

$$\overline{S_{\Delta_-}}(f)^{1/2} = \frac{\sqrt{3E_+{}^2 + E_{DC}{}^2}}{2kM|E_2|E_+} \frac{(1-r_3 r_4)^2}{T_3 r_4} \sqrt{1+\left(\frac{2\pi f}{\omega_c}\right)^2} \tag{5}$$

The signals which are used to control the common mode arm length and the beam splitter may also be shot noise limited at higher frequencies. An estimate of their shot noise limited sensitivity can be found in a relatively straightforward manner from the shot noise limit for the differential mode given in Eq. (5). The shot noise limited sensitivity to common mode motion will have the same frequency dependence as the shot noise limit for the differential motion while the beam splitter shot noise limit is flat. This is because the shape of the shot noise curves are the inverse of the sensitivity curves.

We can approximate the ratio between the DC sensitivities to common mode and differential mode motion by scaling by the powers falling on the two detectors and the sensitivity of each detector to phase variations in the sensed degree of freedom. P_S is the power of the light returning to the laser which is deflected by an optical isolator and P_A is the power of the light exiting the antisymmetric port. We also define η_S and η_A as the quantum efficiencies of the corresponding photodiodes. These quantum efficiencies include the effects of the attenuators and other optics placed before the photodiode. The signal sensing the Φ_+ degree of freedom is proportional to $\eta_S\, \partial v_1/\partial\Phi_+$, and the signal sensing the ϕ_- degree of freedom is proportional to $\eta_S\, \partial v_3/\partial\phi_-$. The shot noise on the symmetric port photodiode, which senses both the common mode and beam splitter motion, is proportional to $\sqrt{\eta_S P_S}$. Using the analogous relations for the differential mode degree of freedom we find

$$\left(\frac{S_{\Phi_+}(0)}{S_{\Phi_-}(0)}\right)^{\frac{1}{2}} \approx \left(\frac{P_S}{P_A}\right)^{\frac{1}{2}} \left(\frac{\eta_A}{\eta_S}\right)^{\frac{1}{2}} \frac{\partial v_3/\partial\Phi_-}{\partial v_1/\partial\Phi_+} \tag{6}$$

$$\left(\frac{S_{\phi_-}(0)}{S_{\Phi_-}(0)}\right)^{\frac{1}{2}} \approx \left(\frac{P_S}{P_A}\right)^{\frac{1}{2}} \left(\frac{\eta_A}{\eta_S}\right)^{\frac{1}{2}} \frac{\partial v_3/\partial\Phi_-}{\partial v_2/\partial\phi_-} \tag{7}$$

where $S_{\Phi_+}^{1/2}$ is the shot noise limited sensitivity to the Φ_+ degree of freedom and similarly for $S_{\Phi_{-+}}^{1/2}$ and $S_{\phi_-}^{1/2}$.

Shot noise in the auxiliary signals sets a lower bound on the residual motion of the auxiliary degrees of freedom in the gravitational wave band. The feedthrough of motion in the auxiliary degrees of freedom to the v_3 signal sets a corresponding lower bound on the gravitational wave displacement sensitivity. This limit could in general be above or below the limit set by shot noise in the v_3 signal itself. Let us define $S_{\Phi_+ \to \Phi_-}(f)^{1/2}$ which is the shot noise limited sensitivity to differential mode motion due to shot noise in the common mode signal. Analogously, we define $S_{\phi_- \to \Phi_-}(f)^{1/2}$.

$$\left(\frac{S_{\Phi_+ \to \Phi_-}(0)}{S_{\Phi_-}(0)}\right)^{\frac{1}{2}} = \left(\frac{S_{\Phi_+}(0)}{S_{\Phi_-}(0)}\right)^{\frac{1}{2}} \frac{\partial v_3/\partial\Phi_+}{\partial v_3/\partial\Phi_-} \approx \left(\frac{P_S}{P_A}\right)^{\frac{1}{2}} \left(\frac{\eta_A}{\eta_S}\right)^{\frac{1}{2}} \frac{\partial v_3/\partial\Phi_+}{\partial v_1/\partial\Phi_+} \tag{8}$$

$$\left(\frac{S_{\phi_- \to \Phi_-}(0)}{S_{\Phi_-}(0)}\right)^{\frac{1}{2}} \approx \left(\frac{P_S}{P_A}\right)^{\frac{1}{2}} \left(\frac{\eta_A}{\eta_S}\right)^{\frac{1}{2}} \frac{\partial v_3/\partial\phi_-}{\partial v_2/\partial\phi_-} \tag{9}$$

(10)

Contrast Defect

The contrast defect is an important parameter in determining the interferometer performance, particularly the shot noise limited sensitivity. From our definition of contrast in Eq. (1), we can write the contrast defect,

$$1 - C = \frac{2P_D}{P_B + P_D} \approx \frac{2P_D}{P_B} \tag{11}$$

The contrast can be degraded by rms motion of the beam splitter, different visibilities in the two arms, alignment errors, and the asymmetry.* Here we consider each of these effects in turn and use these results in Section III to set limits on the resulting contrast defect.

The contrast defect can be degraded by low frequency motion of the beam splitter if it is not sufficiently well controlled. With the arm cavities in perfect resonance, assuming negligible losses in all the optical elements, the power transmission from the laser input beam to the anti-symmetric port is $\sin^2(\phi_-/2)$. For small contrast defects, the contribution to contrast defect due the rms motion of the beam splitter is given by:

$$\sin^2\left(\frac{\phi_-^{\mathrm{rms}}}{2}\right) \approx \frac{1}{2}(1 - C) \tag{12}$$

---

* The contrast could, in principle, also be degraded by distortions in the optical phase front due to imperfect optics. With the high quality optics in the 40-m inteferometer, this effect is negligible.

If the arm cavities have different visibilities, the difference in the amount of light returning from the each arm will cause a contrast defect. The field returning from the in-line arm to the antisymmetric port is:

$$E_5 = r_2 t_2 \sqrt{1 - V_1}\, E_0 \tag{13}$$

where r_2 and t_2 are the amplitude reflectivity and transmission of the beam splitter, V_1 is the visibility of the in-line arm cavity in the limit of zero modulation* and E_0 is the field incident on the beam splitter. The field returning from the perpendicular arm is opposite in phase so that the field at the antisymmetric port is:

$$E_A = r_2 t_2 (\sqrt{1 - V_1} - \sqrt{1 - V_2})\, E_0 \tag{14}$$

The contrast defect then is,†

$$1 - C \approx 2 \left|\frac{E_A}{E_0}\right|^2 = 2 R_2 T_2 \left|\sqrt{1 - V_1} - \sqrt{1 - V_2}\right|^2 \tag{15}$$

An angular tilt of the beam axis for the beam returning from one arm will cause imperfect interference at the beam splitter. This could be caused by orientation noise of the test masses or beam splitter. An angular tilt θ will cause the phase fronts of the interfering beams from the two arms to no longer be parallel and the spot positions to be shifted relative to each other. If the output mode of the cavity with the tilted beam axis is expressed in terms of the modes of the untilted cavity, for small tilts the output mode can be approximated as:[15]

$$E' \approx A\left[\mathrm{TEM}_{00} + i\,\frac{\pi\,\theta\,w_0}{\lambda}\,\mathrm{TEM}_{01}\right] \tag{16}$$

where A is the amplitude of the original TEM_{00} mode. This approximation is valid when $(2\pi\theta w_0)/\lambda \ll 1$, which says that the tilt angle is much less than the far-field divergence angle of the beam. It is only the TEM_{01} piece which will not interfere destructively at the antisymmetric port. We define the fractional power of this non-interfering part due to the non-parallel phase fronts as

$$k_1 = \left(\frac{\theta\,\pi\,w_0}{\lambda}\right)^2 \tag{17}$$

---

* The phase modulation will decrease the measured arm cavity visibilities. Contrast defect is defined with respect to power in the carrier, so it is the zero modulation depth limit which is important here.

† Note that the reflectivity and transmission of the beam splitter affects the resulting contrast defect but does not cause it. In fact, the greater the beam splitter unbalance between reflectivity and transmission, the smaller the contrast defect for a given arm cavity visibility mismatch.

The motion of the spot position also couples some of the light returning from the tilted arm into a higher order mode in the basis of the untilted arm. The fraction that does not interfere due to spot position movement is

$$k_2 = \left(\frac{l\theta}{w_0}\right)^2 \tag{18}$$

where l is the distance between the input test mass and the beam splitter. We assume that $l \ll R$, where R is the radius of curvature of the beam. The fraction of the light incident on the interferometer which returns to the beam splitter is $(1 - V)$ where V is the average arm cavity visibility. Thus the contrast defect induced by alignment errors in the beam returning from one arm is approximately,

$$1 - C \approx 2(1 - V)(k_1 + k_2) \tag{19}$$

The asymmetry induces a contrast defect because the positions of the waists of the beams returning from the two arms are different. Thus at the beam splitter, the transverse size and curvature of the modes returning from the two arms are not identical. Expanding the modes of the farthest arm from the beam splitter in terms of the modes of the closest one, we can approximate that the light returning from it as:

$$E' \approx A\left[\mathrm{LG}_{00} + \frac{\lambda\delta}{2\pi w_0^2}\,\mathrm{LG}_{10}\right] \tag{20}$$

where LG_{00} and LG_{10} are the lowest order Laguerre-Gaussian radial modes[*]. This approximation is valid in the limit that $(\lambda\delta)/(\pi w_0^2) \ll 1$. Thus the contrast defect due to the asymmetry is

$$1 - C \approx 2(1 - V)\left(\frac{\lambda\delta}{2\pi w_0^2}\right)^2 \tag{21}$$

III Experiment

The primary goals of the experimental program with the recombined interferometer were to demonstrate and study lock acquisition in a suspended interferometer using the asymmetry signal extraction scheme, to understand the noise sources limiting interferometer performance, to provide further validation of the asymmetry signal extraction scheme model, and to give information useful for modification of the 40-m interferometer to a recycled configuration. All of these goals,

---

[*] It is most convenient to use polar coordinates and Laguerre-Gaussian modes when considering changes in waist size and position along the beam axis.

with the exception of a complete characterization of the noise, were met. Because the noise limiting the gravitational wave signal is not fully understood, complete descriptions of the noise sources eliminated as candidates are given. Several sources of displacement noise affecting the test masses have been well studied in the Fabry-Perot interferometer and have been shown not to limit the gravitational wave signal.[16,17] Since these sources of noise are not increased in a recombined configuration, we shall not consider them here.

One expects that the sensitivity to various sensing noise sources could change in the recombined configuration. Thus, careful attention is paid to shot noise, intensity noise and frequency noise of the light. The investigation of these noise sources was complicated by the fact that laser system was replaced during the recombination task. When the gas tube in the original laser reached the end of its service life, it was decided to replace the entire laser system with another system with improved automation and operator control features. The intensity noise of the replacement laser system was later shown to be higher than the original system. With the original laser system the interferometer noise was not limited by shot noise, intensity noise or frequency noise. With the replacement laser system, the interferometer was limited by intensity noise above 500 Hz.

Servo Configuration

A block diagram of the servo loops used to control the longitudinal degrees of freedom of the recombined interferometer is shown in Figure 8. The south arm, which receives light reflected from the beam splitter, is shown in its position in the figure for ease of drawing. The loop shapes of all the servo loops were designed to suppress the low frequency, seismically driven motion of the suspended optics to maintain them at their optimum operational points. At the same time the servo loops must not degrade the noise performance at higher frequencies where their sensor noise is higher than the ambient motion.

The common mode (CM) error signal contains the difference between the laser frequency and average resonant frequency of the two arms. The CM servo fed back to the laser system so that the laser frequency tracked the average arm cavity length, except at very low frequencies. Below approximately 3 Hz the error signal was used to correct the average position of the end masses through the recombination coil driver.

The differential mode (DM) servo controlled the two arm cavity lengths so that they maintained the same resonant frequency. The difference signal was fed back to the recombination coil driver to adjust the positions of the end masses.

The recombination coil driver drove magnetic coils mounted near magnets glued onto the rear test masses. These were used to control the length of the arm cavities. The recombination coil driver received input from the CM and DM servo electronics and its outputs, A1 and A2, were linear combinations of its inputs:

$$\begin{aligned} A1 &= CM + DM \\ A2 &= CM - DM \end{aligned} \tag{22}$$

The beam splitter was controlled by four magnets glued onto it, three in a triangular configuration on one face and one on its side to dampen side to side motion. These magnets were driven by optically sensed electromotors (OSEMs) which ensure that the magnet remains in a fixed position in the middle of the coil surrounding it by use of an LED shadow sensor. The beam splitter

OSEM control module also included provisions to allow a more sensitive alignment and longitudinal drive signals to be summed into the signal driving the three coils on the face of the beam splitter. The longitudinal drive signal was provided by the beam splitter servo amplifier.

Each of the three longitudinal servo loops had independent phase shifters to adjust the phase of the demodulation signal. These were adjusted to maximize the desired error signal.

The box marked “LASER System” on Figure 8 includes the laser, optics and servo systems to provide frequency and intensity stabilized laser light to the interferometer. A more detailed drawing of the laser system alone is shown in Figure 9. The laser system provides frequency stabilized light, independent of the interferometer, by controlling the laser frequency to match the resonant frequency of a reference cavity. Since the light passing through this cavity is used by the interferometer, the cavity also provides some spatial filtering of undesirable higher order modes and reduces intensity fluctuations. In this capacity the reference cavity is called a mode cleaner cavity. The feedback to the laser frequency is actuated by moving the laser mirrors (one with large dynamic range and slower response and one with faster response and lower dynamic range) and by frequency shifting the light at high frequencies with a Pockel’s cell. The free running laser has a typical line width of 3 MHz which is reduced to roughly 30 Hz after being locked to the reference cavity. The bandwidth of the laser servo is approximately 1 MHz and it has a gain of 10^9 at low frequencies. This gain suppresses the laser frequency noise to the noise level of the reference cavity.

Notice that there are actually two feedback paths from the common mode servo to the laser frequency. As mentioned above, at frequencies below 3 Hz the common mode error signal is used to control the average of the two arm cavity lengths. At frequencies from 3 Hz to a few kHz, the error signal is used to control the length of the reference cavity. At frequencies above this to several hundred kHz, the common mode signal is summed directly into the laser servo.

Power stabilization of the laser light is also provided by a power stabilization servo. A small fraction of the light directly before the beam splitter is diverted to a photodiode. The difference between the power on this photodiode and a reference level is used to control an acousto-optic modulator which diverts power out of the laser beam to maintain a constant power level incident on the beam splitter. For diagnostic purposes an independent and low noise photodiode is available as well to monitor a fraction of the light incident on the beam splitter.

Lock Acquisition

The largest concern before the operation of the recombined interferometer was the undefined mechanism for acquiring lock. When the interferometer is in a stable situation, where both of its arm cavities are being held very close to resonance by the common and differential mode servos and the beam splitter is being held such that there is a dark fringe at the antisymmetric port, we say the interferometer is “in lock.” The states the interferometer passes through in going from all the optics swinging freely to being in lock are part of the lock acquisition process. The fundamental problem is that the Fabry-Perot cavities using RF reflection locking techniques only provide a signal which is linearly proportional to their length for very small deviations from resonance. In a suspended interferometer where the mirrors are swinging through many fringes at the pendulum resonance frequency, the signal used to adjust these mirror positions will often be zero or of the wrong sign.

Time domain models which include the nonlinear dynamics of the lock acquisition process have been developed by others in parallel with this work. The understanding gained from the model of a single Fabry-Perot cavity was complete enough, in fact, for a computer controller to decrease the lock acquisition time of a single cavity by an order of magnitude.[18] The model for a recombined or more complicated interferometer, however, was not far enough along to be useful in predicting the lock acquisition behavior of the 40-m interferometer, prior to commencement of this experimental program.

The lock acquisition sequence observed was that the beam splitter acquired lock first, because of its very broad range of linear operation, and held the antisymmetric port on a dark fringe. The common mode servo would then acquire lock and hold one of the arm cavities on resonance. Because this servo has a very high bandwidth, we expect it to acquire before the differential mode. With one arm cavity on resonance and one off resonance, the signal read by the common mode servo was almost entirely due to the arm on resonance. The arm that was swinging freely would pass through a resonant condition several times a second. While passing through resonance the out of lock arm would contribute to the common mode signal comparably to the in lock arm. It was a pleasant surprise that this typically did not disrupt the resonance of the arm in lock. When the relative velocity of the test masses in the out of lock arm was low enough as this arm passed through resonance, the differential mode servo was able to lock onto that fringe. This was in fact very similar to the situation we had with the Fabry-Perot interferometer where one arm would acquire lock easily and we would have to wait an average of several minutes for the feedback to the mirror positions of the other arm to catch and hold it on a resonance condition.

Although it would seem that both arms should have been selected with equal probability to be the initial arm in lock, in fact it was much more commonly the south arm that locked first. This is most likely due to the fact that the beam splitter is unbalanced such that 20% more light goes to the south arm than the east arm, and that the south arm has higher optical gain because its losses are lower. This may also help explain why the east arm passing through resonance would not disturb the lock of the south arm. In the cases where the east arm did acquire lock first, the south arm was often successful in “stealing” the common mode lock when it later passed through resonance.

Validation of the Matrix of Discriminants

A goal of recombination was to provide further validation of the models developed for the asymmetric signal extraction scheme. In particular, we wish to verify experimentally the matrix of discriminants. This is quite difficult in practice because the matrix of discriminants which describes the optical response of the interferometer can only be measured when the interferometer is being actively controlled by servo loops to keep it in a linear region of operation. Because there is a large degree of cross coupling between the various extracted signals and degrees of freedom, we must treat the interferometer as a MIMO system in calculating the effect of the servo loops on our measurement.

Closed Loop Measurements

We made the closed-loop response measurements shown in Figure 20. Note that the block elements representing electrical or optical transfer functions are matrices and that the signals shown are vectors containing information on all three servo loops.[*] The interferometer response, *P*, is the matrix of discriminants we wish to verify. The other matrices are various parts of the

---

[*] We use the same notation as previously: the first element of a vector is the common mode signal, the second is the beam splitter signal and the third is the differential mode signal.

servo loops and are diagonal or very nearly diagonal. We injected a signal into the servo loops one at a time at 132.5 Hz at summing point *d*, and observed the disturbance actually present in the loop at point *x*, immediately before the transducer which converts the servo signal to displacement of that degree of freedom. We also observe the signals induced at our drive frequency in all three servos at the outputs of the three mixers, y_i. 132.5 Hz was chosen because it was a relatively quiet area of the noise spectrum for all three degrees of freedom. The power spectrum of the *x* and *y* signals were measured using an HP 3563A Spectrum Analyzer and the values at 132.5 Hz were divided to compute the magnitude of the transfer function from *x* to *y* at this frequency.

The closed loop response to driving the common mode had to be corrected by a measured loop gain factor. This is because unlike the beam splitter and differential mode servos, the common mode has three different feedback paths. At very low frequencies below a few Hz, it drives the test masses directly. At higher frequencies the drive to the test masses is inactive and the feedback is applied to the laser frequency instead, through the remaining two feedback paths. Unfortunately the only feedback path in the common mode servo where we have a solid calibration of voltage to displacement is the drive to the test masses. It is not practical to make the measurements described here at frequencies where this is the dominant feedback path because they would be swamped by seismic noise. Thus we are forced to account for the effects of the other feedback paths in the measurements that involve driving the common mode degree of freedom.

Consider the simplified block diagram of the common mode servo shown in Figure 21. Here the common mode servo is modeled as being composed of only two feedback paths, one fast and one slow. The open loop gains of each of the feedback paths add to form the open loop gain of the entire servo.

$$\frac{x}{d} = \frac{P}{1 - PC_1 - PC_2} \tag{23}$$

$$\frac{q}{d} = \frac{1 - PC_2}{1 - PC_1 - PC_2} \tag{24}$$

The transfer function measured in determining the common mode to common mode response was from *q* to *x*.

$$\frac{x}{q} = \frac{x}{d}\left(\frac{q}{d}\right)^{-1} = \frac{P}{1 - PC_2} \tag{25}$$

We wanted to measure *P*, but it was suppressed by the gain of the faster part of the servo loop. This is true for the off-diagonal matrix element measurements as well because the real common mode change induced is much less than that measured by looking at the drive to the test masses. The fast servo suppresses this motion by changing the frequency of the light to compensate. Thus we have to correct all the measured interferometer responses to driving the common mode by multiplying them by $1 - PC_2 \approx 1 - L_1$, where L_1 is the common mode open loop gain.

Calculated Closed Loop Response

Referring again to Figure 20, we can calculate the expected interferometer response by considering the closed-loop matrix equations:

$$y = BPACq \qquad q = r + d \qquad r = Dy \tag{26}$$

$$y = BPACDy + BPACd \tag{27}$$

$$y = (I - BPAG)^{-1} BPACd \tag{28}$$

where *I* is the identity matrix and $G = CD$. Now to solve for *x* in terms of *d*, we note

$$y = BPAx \rightarrow x = (BPA)^{-1} y \tag{29}$$

$$x = (BPA)^{-1}(I - BPAG)^{-1} BPACd \tag{30}$$

Now for a particular response measurement from loop *j* to loop *k*,*

$$\begin{aligned} y_k &= [(I - BPAG)^{-1}]_{\text{row } k}\, BPACd \\ x_j &= [(BPA)^{-1}\,(I - BPAG)^{-1}\,]_{\text{row } j}\, BPACd \end{aligned} \tag{31}$$

For each measurement where we observe x_j, we inject a signal at 132.5 Hz only into that servo. Thus, only the *j*th element of *d* will be non-zero and this will pick out the *j*th column of *BPAC*.

$$\frac{y_k}{x_j} = \frac{[(I - BPAG)^{-1}]_{\text{row } k}\,[BPAC]_{\text{col } j}}{[(BPA)^{-1}\,(I - BPAG)^{-1}\,]_{\text{row } j}\,[\,BPAC]_{\text{col } j}} \tag{32}$$

Now we exploit the fact that *C* is a diagonal matrix. For any matrix *M* and diagonal matrix *C*:

$$[MC]_{\text{col } j} = M_{\text{col } j}\, C_{j,j} \tag{33}$$

$$\begin{aligned} \therefore \frac{y_k}{x_j} &= \frac{[(I - BPAG)^{-1}]_{\text{row } k}\,[BPA]_{\text{col } j}}{[(BPA)^{-1}\,(I - BPAG)^{-1}\,]_{\text{row } j}\,[BPA]_{\text{col } j}} \\ &= \frac{[(I - BPAG)^{-1}\,BPA]_{k,j}}{[(BPA)^{-1}\,(I - BPAG)^{-1}\,BPA]_{j,j}} \end{aligned} \tag{34}$$

This gives us a way to relate our calculated matrix of discriminants to experiment. We first measure y_k/x_j for all combinations as shown in Figure 20. Then we measure *A*, *B* and *BPAG* and use Eq. (34) to calculate the effect of the servo loops in converting the theoretical matrix of discriminants, *P*, to expected values for y_k/x_j. We ultimately renormalize all our y_k/x_j such that the

---

* We make use of the following matrix identities which are true for any matrices *A* and *B* and vector *x*:

$$[AB]_{\text{row } j} = A_{\text{row } j}\, B \qquad [Ax]_{\text{row } j} = A_{\text{row } j}\, x$$

differential mode drive to differential mode mixer output is 1.0, just at we did for the matrix of discriminants. Thus what is important for all the matrices is the ratio of the various elements and not their absolute size in any particular units.

Measuring the Gain Matrices

The A matrix gives the displacement transducer responses. We assume the response for the common mode and differential mode are equal as they drive the same coils at the two end test masses. The common mode drive voltage was measured by summing together the signals from the recombination coil driver going to each end test mass. Similarly the differential mode drive voltage was measured by taking a difference of these signals.

The conversion from drive voltage to displacement of the test masses is measured by driving an end mass at 10 Hz through several arm cavity resonances. The motion induced is far above the ambient motion at this frequency. By monitoring the reflected light from the arm cavity, the points when it passes through resonance every one-half of the laser wavelength can be seen. By measuring the differences in the drive voltages on a storage scope between successive resonances and averaging over many such measurements, once can determine the voltage necessary to push the test mass $\lambda/2$ at the drive frequency. Because the test mass is suspended as a pendulum, this calibration rolls off as f^{-2} above the pendulum resonance frequency. The voltage to displacement calibration used here is[*]

$$x(f) = \left(5.39\times10^{-6}\ \frac{\mathrm{m\ Hz}^2}{\mathrm{V}}\right)\frac{V_{\mathrm{tm}}}{f^2} \tag{35}$$

where V_{tm} is the drive voltage to the test mass. The cross coupling of the common and differential mode inputs of the recombination coil driver was also measured and included as off-diagonal elements in the A matrix. The beam splitter drive voltage to displacement calibration was measured in an analogous way to be

$$x(f) = \left(4.28\times10^{-6}\ \frac{\mathrm{m\ Hz}^2}{\mathrm{V}}\right)\frac{V_{\mathrm{bs}}}{f^2} \tag{36}$$

where V_{bs} is the voltage fed back to the beam splitter OSEM module position input. After renormalizing,

$$A = \begin{bmatrix} 1.0 & 0 & 1.3\times10^{-3} \\ 0 & 1.3 & 0 \\ 7.1\times10^{-3} & 0 & 1.0 \end{bmatrix} \tag{37}$$

Matrix B is the product of the transmission of the optical path from the beam splitter to the antisymmetric or symmetric port photodiode, the efficiency of the photodiodes and the gains of

---

[*] The uncertainty in this calibration is approximately 20%.

the mixers. The transmission from the beam splitter to the antisymmetric port is 1.77 times higher than the transmission to the symmetric port. This is because the symmetric port light travels back through a number of optics including the Faraday isolator before reaching the photodiode. To measure the efficiency of the photodiodes and the mixer gains together, a sine wave at very close to the 12.33 MHz modulation frequency was injected into the photodiodes' test inputs. This adds the signal in directly across the photodiode and is equivalent to light producing a photocurrent at this frequency.* Each photodiode output is demodulated at a mixer as usual and the resulting peak height in the spectrum of the mixer output is compared with the heights from the other mixers. The frequency of the injected signal is adjusted to give a demodulated peak close to the frequency of interest. The mixer outputs had peak heights at the same injected signal level of -73.614 $\mathrm{dBV_{rms}}$ for the v_1 signal, -75.0 $\mathrm{dBV_{rms}}$ for the v_2 signal, and -63.139 $\mathrm{dBV_{rms}}$ for the v_3 signal. Thus, multiplying these relative gains together and renormalizing,

$$B = \begin{bmatrix} 1.17 & 0 & 0 \\ 0 & 1.0 & 0 \\ 0 & 0 & 6.93 \end{bmatrix} \tag{38}$$

To form the matrix product *BPAG*, we need to measure *G*. *G* is a diagonal matrix representing the electronic gain of the components in each servo loop not included in *A* or *B*. Instead of measuring *G* directly, we measure the open loop gain of each servo loop at 132.5 Hz and form

$$G_{ij} = \begin{cases} \dfrac{L_i}{B_{ii} P_{ii} A_{ii}} & i = j \\ 0 & i \neq j \end{cases} \tag{39}$$

where L_i are the open loop gains of the three servo loops. In this way we automatically preserve the correct phase relationships that we may have ignored in only considering the magnitude of the *A* and *B* matrices.

Measuring the open loop gains of the servos controlling the three degrees of freedom is complicated by the fact that the optical part of the servo loops is only linear in its response when the servo loops are closed. Thus to measure the open loop gain of each particular loop, we need to make a closed loop measurement and calculate the effective open loop gain. As shown in Figure 22, we feed a test signal into *d* and measure the transfer function to *x*. In the diagram *P* is the optical part of the gain, while *H* and *G* are the parts of the electronic gain before and after the summing junction respectively. Any convenient summing junction and monitor point that is buffered from it and later in the electronic path may be used, but in practice there are limited choices of test inputs and outputs in the electronic modules. With the loop closed the transfer function from *d* to *x* is

---

[*] The photodiodes have different efficiencies primarily because the photodiode itself is part of an LC circuit which is tuned for 12.33 MHz. The electrical gain from this circuit can vary by up to an order of magnitude from photodiode to photodiode.

$$\left.\frac{x}{d}\right|_{\text{closed loop}} = \frac{G}{1 - GPH} \tag{40}$$

After measuring the closed loop response, we break the servo loop somewhere before the summing junction and after the monitor point, typically by blocking the laser light. Then we remeasure the transfer function from *d* to *x*,

$$\left.\frac{x}{d}\right|_{\text{open loop}} = G \tag{41}$$

We can then find the open loop gain of the servo loop by calculating

$$GPH = 1 - \left.\frac{x}{d}\right|_{\text{open loop}} \Big/ \left.\frac{x}{d}\right|_{\text{closed loop}} \tag{42}$$

Using this procedure we find that at 132.5 Hz,

$$\begin{aligned} L_1 &= 9.368\times10^{4} + i\,2.168\times10^{5} \\ L_2 &= 1.592\times10^{-1} - i\,4.626\times10^{-2} \\ L_3 &= 2.936\times10^{1} - i\,6.903\times10^{-1} \end{aligned} \tag{43}$$

Comparison of Calculated and Measured Interferometer Response

For this comparison we will not use the matrix of discriminants from Table 2 because we can not reasonably expect the beam splitter demodulation phase to be set more accurately than within 10°. For comparison with our data, we use a matrix of discriminants calculated assuming a 10° beam splitter mixer phase error,* which we write as†

$$P = \begin{bmatrix} 7.8 & 2.3\times10^{-4} & 2.5 \\ 1.3 & 1.5\times10^{-4} & 4.0\times10^{-1} \\ 2.2\times10^{-1} & 1.9\times10^{-4} & 1.0 \end{bmatrix} \tag{44}$$

Using this matrix we can calculate the expected interferometer response measurements (y_k/x_j).

---

* Note that the choice of 10° is not critical. The amount of common mode feedthrough depends linearly on the phase error for small phase errors such as these. Negative phase errors give a dependence on the common mode length of equal magnitude to positive errors. Thus, the common mode and differential mode feedthrough to the beam splitter signal which are derived from a 10° phase error are probably good estimates to within an order of magnitude.

† Note that in matrix form this is transposed from how it appears in Table 2 because in the table the inputs (degrees of freedom) appeared as rows and the outputs (extracted signals) appeared as columns for readability.

The calculated interferometer response is shown in Table 6 along with the values measured in the lab. The agreement is within the errors of the measurement except for the upper right block of values.* These discrepancies are discussed below.

The interferometer response to a beam splitter drive was a factor 2 to 2.5 lower than predicted for both beam splitter and differential mode degrees of freedom.† Part of the uncertainty in the magnitude of all the elements on this row of Table 6 is the relative voltage to displacement calibration for the beam splitter versus the test masses which is described by the *A* matrix. Since the common mode and differential mode both drive the test masses, there is little uncertainty associated with the relative sizes of the first and third rows. An additional uncertainty is that the measurement was taken near the unity gain frequency of the beam splitter and so small gain fluctuations in that servo could yield substantially larger fluctuations in its closed loop response.‡

The factor of 10 to 10^4 difference in the common mode to beam splitter and common mode to differential mode measurement have to do with imperfections in the electronics which exploit the unique features of the common mode servo. The problem is that some small amount of the signal injected into the common mode leaks into the differential mode before being suppressed by the common mode servo. As shown in Eq. (37), the fractional common mode to differential mode cross coupling that occurs in the recombination coil driver module is 7.1×10^{-3}.** The cross coupling between the test input, which is used to inject the signal into the common mode servo, and the differential mode is 1.1×10^{-2}. Thus, our assumption in deriving Eq. (34) that we were driving only one servo at a time is not strictly true. In most cases this is not significant, but for the common mode drive (where we have to compensate for the additional feedback paths by multiplying by the common mode loop gain which is 2.4×10^{5} at 132 Hz) this can be a significant source of error.

As an example of the size of this effect, we consider the common mode to differential mode term. A 1 V_{rms} drive into the common mode test input generated a 55.8 mV_{rms} signal in the common mode drive to the masses. Because of the direct cross coupling, the differential mode would have seen an 11 mV_{rms} drive. A 500 mV_{rms} drive produced 60.0 mV_{rms} signal in the differential mode drive to the masses, thus we would expect the cross coupling to produce a 0.13 mV_{rms} drive differentially. Thus purely from the electronic cross coupling in the recombination coil driver we would measure an interferometer differential mode response to common mode drive of 2.37×10^{-2}. After multiplying by the common mode loop gain and normalizing by the differential mode to differential mode response, this would give a common mode to differential mode element in Table 6 of 2.1×10^{2}. This is in reasonable agreement with the number measured, and thus it

---

* Most of the measurement uncertainty comes from the measurement of *G*, *A* and *B* and not from the interferometer response measurements.

† The beam splitter to common mode is given as 0 because the beam splitter could not be excited enough to give a signal in the common mode loop without disrupting the lock. This is consistent with the very weak response predicted by the theory.

‡ The effect of the Doppler shift described is a factor of two correction at 132.5 Hz. Nonetheless, this correction would only serve to increase the predicted interferometer response to beam splitter motion.

** This is the as good as can be expected with 1% resistors.

appears that the signal we are trying to measure is hidden by the much larger effect of leakage into the differential mode.

A similar argument can be constructed for the common mode to beam splitter term. The magnitude of the effect of the common mode test input signal leaking into the differential mode and then being seen at the beam splitter mixer due to differential mode to beam splitter coupling in the interferometer can be estimated by multiplying the common mode to differential mode term in Table 6 by the differential mode to beam splitter term. This gives 8.1×10^{-1} which together with the predicted common mode to beam splitter term gives an improved prediction of 1.0 which is reasonably close to the value observed. Thus we conclude that both of the common mode drive cross terms are dominated by cross coupling from the common mode test input to the differential mode in the recombination coil driver.

Beam Splitter Signal Sign Reversal

A problem with the lock acquisition sequence described above is that the signal to control the beam splitter can reverse sign in going from the case of one arm and the beam splitter in lock to the entire interferometer in lock. This is because the overcoupled Fabry-Perot arm cavities switch the phase of the carrier light reflected from them by $180°$ in going from out of lock to in lock. From Figure 10 we can see that the carrier field at the symmetric port has the same phase with either one or no arms in lock, but reverses when both arms are in lock. Thus in the low modulation depth limit, we expect that if the phase of the beam splitter error signal is originally adjusted to hold the antisymmetric port on a dark fringe with neither arm in lock, then it will of the wrong sign once both arms acquire lock.

In practice this was not observed originally because the mode matching into the arm cavities was poor. Non-mode matched light is reflected directly from the vertex mirrors and does not get phase reversed when the cavity goes into resonance. The non-mode matched fraction of the light was large enough that the phase of all the carrier light reflected from the cavities did not reverse its sign. After improving the mode matching, however, the interferometer was unable to acquire lock at low modulation depth for this reason.

Two schemes for solving this problem were explored. The most straightforward approach is to trigger a sign reversal of the beam splitter feedback signal when both arms go into resonance. After being careful to null out all the offsets in the beam splitter servo, this method was successful. Another method is to increase the modulation depth well above the optimal depth for shot noise limited sensitivity in the gravitational wave signal. As can be seen from Table 3, increasing the modulation depth changed the sign of the beam splitter error signal (v_2) and increased its sensitivity to beam splitter motion without changing the other matrix elements. This is due to a beating between the first and second order sidebands, neither of which experience a phase reversal when the arm cavities go into resonance. In this case the beam splitter has the same sign for its error signal with neither arm in lock and both arms in lock. The method of increasing the modulation depth was the one adopted for most of the tests described here as it worked much more reliably and eliminated some of the noise problems we saw because the sensitivity to beam splitter motion was so small. Because shot noise was not limiting the noise spectrum, running at a non-optimal modulation depth did not limit the sensitivity.

Shot Noise

The differential mode displacement equivalent to shot noise in the gravitational wave readout is estimated using Eq. (5). The parameters for this calculation can be obtained from in-situ measurements of the interferometer, as discussed in reference 14. The resulting estimate of shot noise limited sensitivity is shown in Figure 11. This is compared to an empirical measurement of the shot noise contribution to the gravitational wave signal and to the interferometer displacement spectrum taken at the time these measurements were done. The empirical estimate was accomplished by shining only incandescent light onto the antisymmetric photodiode so that the photocurrent was the same as in normal operation. The resulting signal was calibrated in displacement including the effect of the servo loop gain.

From these results it can be seen that the interometer was not shot noise limited at any frequency. This was confirmed by attenuating signal light on the antisymmetric photodiode and using an incadescent light source to raise the incident power to a factor 3.2 times higher than the original level. If the interferometer were shot noise limited, we would expect a 7 dB increase in the displacement spectrum, but the largest increase seen at any frequency was 4 dB.

The gravitational wave sensitivity limit due to shot noise in the common mode and beam splitter signal can be estimated using Eq. (8) and Eq. (9). The ratio between the power on the symmetric port and the power on the antisymmetric port was typically around 5. As discussed previously, the ratio of quantum efficiencies of the antisymmetric port photodiode to the symmetric port photodiode was approximately 2.[*] Using the matrix elements from Table 2, we estimate

$$\left(\frac{S_{\Phi_+ \to \Phi_-}(0)}{S_{\Phi_-}(0)}\right)^{\frac{1}{2}} \approx 0.09 \tag{45}$$

$$\left(\frac{S_{\phi_- \to \Phi_-}(0)}{S_{\Phi_-}(0)}\right)^{\frac{1}{2}} \approx 3.2 \tag{46}$$

Therefore, we do not expect the shot noise on the common mode signal to limit the gravitational wave sensitivity at any frequency. The shot noise on the beam splitter signal is more problematic, however, and we had to ensure that the open loop gain of the beam splitter servo is less than one in the gravitational wave band. This was considered in designing the loop shape of the beam splitter servo.

To confirm that shot noise on both of these signals was not limiting the gravitational wave sensitivity, we placed an attenuator before the symmetric photodiode to halve the laser light and then used an incandescent light source to increase the power on the photodiode a factor of four. We saw no observable change in the gravitational wave spectrum.

---

[*] These quantum efficiencies include the relative efficiencies of the optical paths to the photodiodes.

Frequency Noise

The imbalance of the arm cavities in the 40-m interferometer greatly reduces its frequency noise rejection over that specified for LIGO. Nonetheless, in the previous Fabry-Perot interferometer, where there is no frequency noise rejection, frequency noise was shown not to limit the gravitational wave signal. Because the servo system controlling the frequency is largely identical in the recombined interferometer, we expected that the recombined interferometer would not be limited by frequency noise. However, since switching to a recombined configuration, the prestabilized laser system was replaced with another system with improved automation and operator control features. Tests to set limits on the frequency noise contribution to the gravitational wave signal were performed both before and after the laser was replaced and were in reasonable agreement.

Since the common mode signal senses laser frequency variations, the test for frequency noise was to inject a monochromatic signal into the common mode servo and observe the resulting peak in both the v_1 signal and in the interferometer output. This test would reveal any form of common mode to differential mode feedthrough, but we expect that frequency noise would dominate. We also expect any common mode to differential mode feedthrough to be essentially constant over some small region around the injected peak. By matching the peak heights and comparing the levels of the ambient backgrounds, we can estimate the common mode contribution to the interferometer output. If frequency noise was actually limiting the interferometer spectrum, the peak-to-valley ratio of common and differential mode signals will be the same. An example of one such measurement is shown in Figure 12.

With the original prestabilized laser, the estimated frequency noise contribution to the interferometer output at 250 Hz was less than $1\times10^{-19}\ \mathrm{m}/\sqrt{\mathrm{Hz}}$ and at 750 Hz was less than $7\times10^{-20}\ \mathrm{m}/\sqrt{\mathrm{Hz}}$.[*] This gives more than 35 dB of margin relative to the interferometer noise. With the new prestabilized laser system, there was also more than 35 dB margin between the estimated frequency noise contribution and the interferometer noise.

Intensity Noise

Intensity noise on the light incident on the interferometer can appear as noise in the gravitational wave readout. Deviations from the arm cavity resonance length increase sensitivity in the gravitational wave signal to intensity fluctuations in the signal band. RF intensity fluctuations can occur even when the arm cavity is exactly in resonance and can be seen directly after being demodulated by the mixers. A number of measurements were performed to determine if noise due to in-band and RF intensity fluctuations were limiting the gravitational wave sensitivity.

There were three methods used to estimate the in-band contribution of intensity noise to the gravitational wave signal. The most straightforward is to do the transfer function measurement from the intensity noise to the interferometer output as shown in Figure 13. A signal is fed into the test input of the intensity stabilization servo and the transfer functions from this point to the interferometer output (G) and to a monitor photodiode (H) are measured. The monitor photodiode is a low noise photodiode which is not part of the intensity stabilization loop. The ratio of these two

---

[*] These numbers are upper bounds because the background noise measured in these measurements was limited by readout noise and not the true servo signal.

transfer functions allows us to infer a transfer function from the noise observed by the monitor photodiode to the interferometer output (G/H). The observed intensity noise is multiplied by this transfer function to derive an estimated contribution to the interferometer output due to intensity noise. The estimated contribution from intensity noise with the original prestabilized laser is shown in Figure 14.

A problem with this method of measuring the intensity noise contribution to the interferometer output is that it requires long integration times at each frequency point. The intensity noise feeds into the gravitational wave signal via deviations from the arm cavity fringe which are time varying around near perfect resonance. In a transfer function measurement, the phase is important and excursions on either side of the fringe give opposite phases in the measurement of G above. Averaged over sufficiently long times, the transfer function measured is that due to the very small static offset from the fringe.

A second method of measuring the contribution of intensity noise to the interferometer output is to inject a monochromatic intensity signal at a level sufficient to increase the noise in the interferometer output at this frequency. By comparing the peak-to-valley ratios of the peak in the interferometer output and in the light measured by the monitor photodiode, we can set a limit on the intensity noise contribution near the frequency of the peak. This has the advantage that the measurements taken are power spectra and thus what is important is the rms deviation from the arm cavity fringe and not the average.* An example of one such measurement using the original prestabilized laser is shown in Figure 15. Notice that the injected peak is broadened in the interferometer output. Depending on the broadening mechanism, this could lead to a falsely low estimation of the intensity noise contribution. The estimated intensity noise contribution using this method at 850 Hz is $3 \times 10^{-19}\ \mathrm{m}/\sqrt{\mathrm{Hz}}$.

A final method for estimating the intensity noise contribution to the interferometer output, which does not suffer from the ambiguity of the broadened peaks, is to inject white intensity noise. White intensity noise was injected at a level to clearly show up in the interferometer output above the ambient noise background. The drive level was then doubled to check for linearity, which did produce a 6 dB increase in the interferometer noise level. Using this method, the intensity noise contribution was $3 \times 10^{-19}\ \mathrm{m}/\sqrt{\mathrm{Hz}}$ at 850 Hz and was relatively flat from 500 - 1000 Hz.

The estimated intensity noise contribution to the interferometer output from the peak-to-valley and white noise methods are in good agreement and set a level of $3 \times 10^{-19}\ \mathrm{m}/\sqrt{\mathrm{Hz}}$ from 500 - 1000 Hz. The estimate for the intensity noise contribution purely from static offsets of the arm cavity fringes (using the transfer function method) is 60 times lower. Thus we can conclude that it was the rms deviation from the fringe that was important for intensity noise.

As part of the characterization of the new prestabilized laser system, the relative intensity noise was measured at 500 Hz and compared to the original system. The original prestabilized laser had a relative intensity noise† of $7 \times 10^{-8}\ \mathrm{Hz}^{-1/2}$ while the new system was measured to have a relative intensity noise of $4 \times 10^{-7}\ \mathrm{Hz}^{-1/2}$. This factor of 6 degradation in performance

---

* RMS excursions enable intensity noise to couple into the interferometer output even when the static offset is zero.

† Relative intensity noise is the square root of the noise power divided by the intensity.

suggests that the intensity noise should limit the gravitational wave sensitivity at some frequencies. A check of this with the new laser system, using the white noise method, showed that the gravitational wave sensitivity was limited by intensity noise above approximately 500 Hz. This was verified with a peak-to-valley measurement at 750 Hz.

A test for RF intensity noise is to misalign all the masses except for one vertex mass so that the light incident on the interferometer is reflected straight back along the same path to the photodiodes. After measuring the demodulated signal at one photodiode (typically the symmetric photodiode), the laser light is blocked and the same amount of power is put on the photodiode with a flashlight. If the intensity noise of the light is shot noise limited around 12 MHz as desired, then the flashlight demodulated signal will be identical to the laser light signal. For both prestabilized laser systems, this was true above 200 Hz. The excess noise that was occasionally seen on the laser light spectrum below 200 Hz was most likely due to a spurious interference path formed between optics in the beam splitter chamber.

Beam Splitter Motion

Beam splitter motion can affect the interferometer output in two ways. The low frequency (less than 10 Hz) rms motion of the beam splitter can degrade the dark fringe at the antisymmetric port. Motions of the beam splitter in the gravitational wave band can also limit the interferometer sensitivity.

To understand the effects of low frequency beam splitter motion, the power spectrum of the residual beam splitter motion was measured and calibrated. An analogous calibration method to that used for the gravitational wave signal could not easily be used because there was no convenient way to sum a signal into the beam splitter position directly at the drive coils.* Instead, the power spectrum of the feedback to the beam splitter drive coils was recorded, and this was converted to the actual residual motion of the beam splitter by measuring the beam splitter open loop gain and making some assumptions about where the noise terms that dominate the beam splitter motion sum into the servo loop.

A schematic diagram of the beam splitter servo loop is shown in Figure 16. The transfer functions from the two types of noise sources are:

$$\frac{x}{d} = \frac{PC}{1-PC} \qquad \frac{y}{d} = \frac{1}{1-PC} \tag{47}$$

$$\frac{x}{e} = \frac{C}{1-PC} \qquad \frac{y}{e} = \frac{C}{1-PC} \tag{48}$$

If the noise source dominating the beam splitter motion is a disturbance (primarily seismic motion), then we can use Eq. (47) to find the relation between the feedback and the actual beam splitter motion,

$$\frac{y}{x} = \frac{1}{PC} \tag{49}$$

---

* With the new test mass suspensions that have been installed in the 40-m interferometer, it is now possible to drive the vertex test masses.

However, if the noise source dominating the beam splitter motion in a particular frequency band is a sensor error (shot noise or electronic noise), then we use Eq. (48) instead to find

$$\frac{y}{x} = 1 \tag{50}$$

We shall assume that the seismic disturbance dominates. This is certainly true in the frequency region below 10 Hz that we are concerned about, which accounts for most of the beam splitter rms motion. Thus we measure the feedback voltage, divide this by the open loop gain of the servo, and then multiply by the conversion from voltage to displacement for the beam splitter drive. The estimated residual beam splitter motion is shown in Figure 18.* The rms motion obtained by integrating this data is 1.34 nm which meets the design specification.

The fluctuations in the beam splitter position at frequencies above 100 Hz can also limit the gravitational wave sensitivity. A check of the beam splitter contribution to the interferometer output revealed that the beam splitter does not limit the gravitational wave sensitivity. The beam splitter motion contribution is measured using a transfer function method as shown in Figure 17. The transfer function from the beam splitter servo test input to the interferometer output (G) is measured first. The transfer function from this test input to the beam splitter feedback signal (H) is also measured. From this the transfer function from the beam splitter feedback to the interferometer output can be inferred by calculating G/H. The ambient power spectrum measured at the beam splitter feedback is then multiplied by this transfer function to find its contribution to the interferometer output. The results of this measurement are shown in Figure 19, plotted for comparison with the best interferometer output sensitivity achieved during operation in the recombined configuration.

Contrast Defect

We typically observed 3% contrast defects after careful alignment, with fluctuations as low as 2%. Using the results of Section II and measured parameters, the various contributions to this are discussed below. The sources of contrast defect considered are rms motion of the beam splitter, differing arm cavity visibilities, alignment fluctuations, and the asymmetry. The budget for the various contributions of contrast defect is summarized in Table 5.†

The rms motion of the beam splitter was shown above to be 1.3 nm, thus $\phi_-^{\mathrm{rms}} = 3.3\times10^{-2}$. Using Eq. (12) we find that this rms beam splitter motion will give 0.05% contrast defect which easily meets the design rms contrast fluctuation requirements.

The visibilities observed in the two arms at low modulation depth when the arms were aligned for maximum transmitted light (and hence maximum circulating power) were 88% for the east arm and 74% for the south arm. This difference is primarily due to the lower mirror losses of the south arm. For the east arm it was noted that in aligning to maximize the visibility, one could

---

[*] As discussed above we expect the low frequency part of this data to be accurately calibrated, although closer to 100 Hz the figure may be in error by as much as the open loop gain of the servo at those frequencies. For this measurement this would correspond to overestimating the motion at 100 Hz by less than a factor of three.

[†] These summarized measurements are taken after the mode matching of carrier light into the arm cavities was optimized.

achieve a visibility of 91%. This is believed to be due to non-uniform losses across the surface of the mirrors. Because the arm cavities are over coupled, aligning for peak visibility may lead to slightly misaligning the cavity so that the resonant spot is on an area of higher loss. For comparison the energy storage time of the east arm aligned for maximum visibility on one particular day was 447 μs while it was 508 μs when aligned shortly afterwards for maximum transmitted light. For this reason the cavities were routinely aligned for maximum transmitted light in normal operation. Using Eq. (15) the contrast defect due to the unequal arm cavity visibilities is 1.3%.

The contrast defect due to alignment fluctuations is given by Eq. (19). As a worst case estimate for the angular tilt in the returning beam axis, we use the orientation noise of the test masses. Thus $\theta_{\text{rms}} \approx 5\times10^{-6}$ rad, or 0.2 mm of spot motion over 40 m. Note that for the 2.2 mm waist size in the 40-m interferometer, the approximations made in deriving Eq. (17) and Eq. (18) are valid. Thus, we calculate the fraction of the light returning from the arms that does not interfere due to the non-parallel phase fronts, $k_1 = 0.45\,\%$, and the fraction that does not interfere due to motion of the beam spot, $k_2 = 0.83\,\%$. The average arm cavity visibility is 81%; therefore, the contrast defect due to angular fluctuations is 0.49%.

The contrast defect arising from the different size and curvature of the modes returning from the two arms due to the asymmetry is given by Eq. (21). For the 50.8 cm asymmetry used, the additional contrast defect is 0.33%.

IV Conclusion

This paper describes the first demonstration of an optical topology in a suspended interferometer which is extensible to the initial LIGO and VIRGO gravitational wave interferometers. Previous efforts at operating a suspended, recombined interferometer did not include Fabry-Perot arm cavities[19] or used hybrid signal extraction schemes where light from each arm was still detected independently.[20,21] The hybrid schemes are closer in similarity to the previous configuration of the 40-m interferometer than to this work. In the recombined configuration described here, three of the four degrees of freedom that will ultimately be needed were shown to be controllable, near the level of precision required in these interferometers. Lock acquisition was shown experimentally to be a tractable problem.

The emphasis of this work was quite different from earlier tabletop demonstrations of recycled interferometers. Rather than demonstrating the general feasibility of the asymmetric control scheme, the focus here was on understanding and accurately modeling the limitations to interferometer performance. To do this, some additional formalism was developed to treat shot noise, contrast defect, and other effects. This formalism has since been used in designing a recycled configuration for the 40-m interferometer.

Most of the experimental results were well described by the initial modeling of the recombined interferometer, although there were surprises. Following our expectations, the interferometer sensitivity was not limited by shot noise on the symmetric photodiode, by frequency and intensity noise of the light or by beam splitter motion. The empirical estimate of the effect of shot noise on the antisymmetric port photodiode was consistent with our calculations. The reasonable agreement between calculated and measured interferometer response functions confirmed our theoretical understanding of the asymmetry signal extraction scheme.

The major limitation to the comparison between measured and calculated interferometer response functions was that the common mode feedback signal was measured at the drive to the test masses which had a gain far less than unity at the frequency of the measurement. This prevented us from accurately measuring the differential mode response to a common mode drive. However, an independent measurement of the common mode contribution to the differential mode noise showed that it was at least 35 dB less than the observed noise. Thus we conclude that despite our inability to accurately measure this matrix element, it is not large enough to limit the performance of the interferometer.

Perhaps the largest surprise of the experimental program, and certainly the most pleasant, was the ease of lock acquisition. The fact that the beam splitter and common mode servo could adequately control the beam splitter and one arm of the interferometer while the other arm was swinging through resonance was not anticipated and made the task much easier. It was fortuitous that our initial attempts at lock acquisition were in a state of poor mode matching into the arms. The sign reversal of the beam splitter control signal at lower modulation depths when moving from one arm in lock to both arms in lock was not appreciated before the experiment. This might have significantly complicated the process of lock acquisition initially, had the mode matching been better.

A large concern before the start of the recombination program was the very large off-diagonal elements in the matrix of discriminants. The imbalance in beam splitter reflectivity and transmission and unequal losses in the two arms mixed the common and differential mode signals to a larger extent than in the tabletop prototype. The responses of the arm cavities in the tabletop prototype was dominated by the large (3%) transmission of the input mirrors, while in the recombined 40-m interferometer they were dominated by the losses in the arms which showed more variability. In addition, the low sensitivity to beam splitter motion in the signal used to control it raised serious concerns about the effects of shot noise and cross coupling with the common mode signal. All of these effects were carefully treated in calculations beforehand, and the prediction that these effects would not seriously degrade the interferometer performance was generally confirmed.

The fact that the interferometer was not shot noise limited was a mystery as no other noise source was found at the time to explain it. The interferometer noise was shown to be approximately a factor of two above the limit from shot noise on the antisymmetric photodiode. It was unfortunate that further work on this part of the frequency band was hampered by the replacement laser system whose higher intensity noise limited the interferometer sensitivity above 500 Hz. A prime candidate to explain this excess noise is scattered light, most likely in the vertex area. For instance, additional light that is scattered onto the antisymmetric photodiode and provides a spurious interferometer path may be one possible mechanism to explain the noise. There is circumstantial evidence to support this view. In laying out the optical paths to the photodiodes, it was found that the interferometer noise was raised by the insertion of a lens in front of the antisymmetric port photodiode, and that additional steering mirrors to these diodes could similarly affect the noise. Also, in measuring the amplitude of the modulation sidebands at the antisymmetric port with a Fabry-Perot optical spectrum analyzer, it was found that reflecting light back into the interferometer raised the overall noise level significantly with a spectral shape similar to the observed noise at high frequencies. In fact, any white noise source at the antisymmetric port photodiode would have this spectral shape after being filtered by the servo loop and readout filters.

It could be said that the primary goal of this work was to establish that many of the problems of operating an interferometer similar to the proposed initial LIGO detectors are tractable.

Although there are issues remaining to be resolved by the recycled 40-m interferometer, many of the most troubling concerns have been settled.

Acknowledgments

We would like to thank the members of the LIGO project for their encouragement and helpful discussions during this work. LIGO is supported by the National Science Foundation under Cooperative Agreement PHY9210038.

References

1. A. Abramovici, et. al., Science **256**, 325 (1992).
2. C. Bradaschia, et. al., Nucl. Instrum. Methods A **289**, 518 (1990).
3. K. Danzmann, et. al., “GEO 600. A 600m Laser Interferometric Gravitational Wave Antenna,” *Proceedings of the First Edoardo Amaldi Conference on Gravitational Wave Experiments*, ed. E. Coccia, G. Pizzella and F. Ronga (World Scientific, Singapore, 1995).
4. G.E. Moss, L.R. Miller, and R.L. Forward, Applied Optics **10** (1971) 2495.
5. R. Weiss, *Quarterly Progress Report of the Research Laboratory of Electronics of the Massachusetts Institute of Technology*, **105** (1972) 54.
6. R.L. Forward, Phys. Rev. D **17** (1978) 379.
7. R.W.P. Drever, G.M. Ford, J. Hough, I.M. Kerr, A.J. Munley, J.R. Pugh, N.A. Robertson, and H. Ward, “A Gravity-Wave Detector Using Optical Cavity Sensing,” 9th International Conference on General Relativity and Gravitation at Jena, GDR (1980).
8. R.W.P. Drever, in *Gravitational Radiation*, ed. N. Deruelle and T. Piran (North Holland, Amsterdam, 1983), 321.
9. M.W. Regehr, *Signal Extraction and Control for an Interferometric Gravitational Wave Detector,* Ph.D. Thesis, California Institute of Technology, 1995.
10. J.A. Giaime, *Studies of Laser Interferometer Design and a Vibration Isolation System for Interferometric Gravitational Wave Detectors*, Ph.D. Thesis, Massachusetts Institute of Technology, 1995.
11. T.T. Lyons, *An Optically Recombined Laser Interferometer for Gravitational Wave Detection*, Ph.D. Thesis, Cal-

ifornia Institute of Technology, 1997.

12. D. Shoemaker, J. Giaime, F. Raab, M. Regehr, and L. Sievers, “Comparison of 2 Fixed Mass Interferometer Testbeds and the Resulting Recommendation for the Initial LIGO Interferometer Design,” Internal LIGO document (1993).
13. R.E. Spero, “In-Situ Measurement of Cavity Parameters Needed for Calculating Shot Noise,” Internal LIGO document LIGO-T940065-00-R (1994).
14. T.T. Lyons, M.W. Regehr, F.J. Raab, “Shot Noise in Gravitational-Wave Detectors with Fabry-Perot Arms”, submitted to Applied Optics, 1999.
15. D.Z. Anderson, Applied Optics **23** (1984) 2944.
16. A. Abramovici, W. Althouse, J. Camp, D. Durance, J.A. Giaime, A. Gillespie, S. Kawamura, A. Kuhnert, T. Lyons, F.J. Raab, R.L. Savage, Jr., D. Shoemaker, L. Sievers, R. Spero, R. Vogt, R. Weiss, S. Whitcomb, and M. Zucker, Phys. Let. A **218** (1996) 157.
17. A.D. Gillespie, *Thermal Noise in the Initial LIGO Interferometers*, Ph.D. Thesis, California Institute of Technology, 1995.
18. J. Camp, L. Sievers, R. Bork, and J. Heefner, Optics Letters **20** (1995) 2463.
19. D. Schnier and K. Danzmann, “Recycling of light power and external modulation on the Garching 30m Interferometer with suspended optical components,” Verhandl. DPG (VI) 31, Q 11.2 (1996).
20. M.-K. Fujimoto, M. Ohashi, T. Yamazaki, M. Fukushima, A. Araya, K. Tsubono, N. Mio, and S. Telada, “Development of a 20m Prototype Laser Interferometric Gravitational Wave Detector at NAO,” in *Proceedings of the First Edoardo Amaldi Conference on Gravitational Wave Experiments*, ed. E. Coccia, G. Pizzella and F. Ronga (World Scientific, Singapore, 1995).
21. G.A. Kerr, *Experimental Developments towards a Long Baseline Gravitational Radiation Detector*, Ph.D. Thesis, University of Glasgow, 1986, pp. 117-130.

Tables

Table 1: Parameters for the 40-m Interferometer

Quantity	Symbol	Value
Mirror (power) transmissions	T_2	0.45
	T_3	280 ppm
	T_5	300 ppm
	T_4, T_6	12 ppm
Loss in each mirror	L_3, L_4	110 ppm
	L_5, L_6	56 ppm
Asymmetry	δ	50.8 cm
Modulation frequency	f_{mod}	12.33 MHz
Modulation index	Γ	1.49
Contrast defect	$1 - C$	0.03

.

Table 2: Extracted Relative Signal Sensitivities

	∂v_1	∂v_2	∂v_3
$\partial\Phi_+$	-7.8	0	-2.2×10^{-1}
$\partial\phi_-$	2.3×10^{-4}	1.9×10^{-4}	-1.9×10^{-4}
$\partial\Phi_-$	2.5	1.6×10^{-8}	1.0

Table 3: Extracted Signal Sensitivities at Different Γ

	∂v_1		∂v_2		∂v_3	
Γ	0.7	1.49	0.7	1.49	0.7	1.49
$\partial\Phi_+$	-7.8	-7.8	0	0	-2.2×10^{-1}	-2.2×10^{-1}
$\partial\phi_-$	2.3×10^{-4}	2.3×10^{-4}	-1.3×10^{-5}	1.9×10^{-4}	-1.0×10^{-5}	-1.9×10^{-4}
$\partial\Phi_-$	2.5	2.5	-2.5×10^{-9}	1.6×10^{-8}	1.0	1.0

Table 4: Parameters Used in Shot Noise Prediction

Name	Value
$V_{\max}$	1.1 V
$V_{\min}$	20 mV
R	50 Ω
Γ	0.705
M	0.77
α ????	0.132
T_3	280 ppm
r_3	0.999805
r_4	0.999938

Table 5: Contrast Defect Contribution Budget

Mechanism	Contribution
RMS beam splitter motion	0.05%
Arm cavity visibilities	1.3%
Alignment fluctuations	0.49%
Asymmetry	0.33%
Total	2.18%

Table 6: Comparison of Calculated (shaded) and Measured (normal) Interferometer Response

Loop Driven	Loop in which Response Measured					
	Common mode (1)		Beam splitter (2)		Differential mode (3)	
1	1.3	1.4	2.0×10^{-1}	1.6	1.9×10^{-2}	2.7×10^{2}
2	2.8×10^{-10}	0	2.2×10^{-5}	1.1×10^{-5}	9.5×10^{-6}	3.8×10^{-6}
3	1.9×10^{-6}	1.9×10^{-6}	2.9×10^{-3}	3.0×10^{-3}	1.0	1.0

Figures

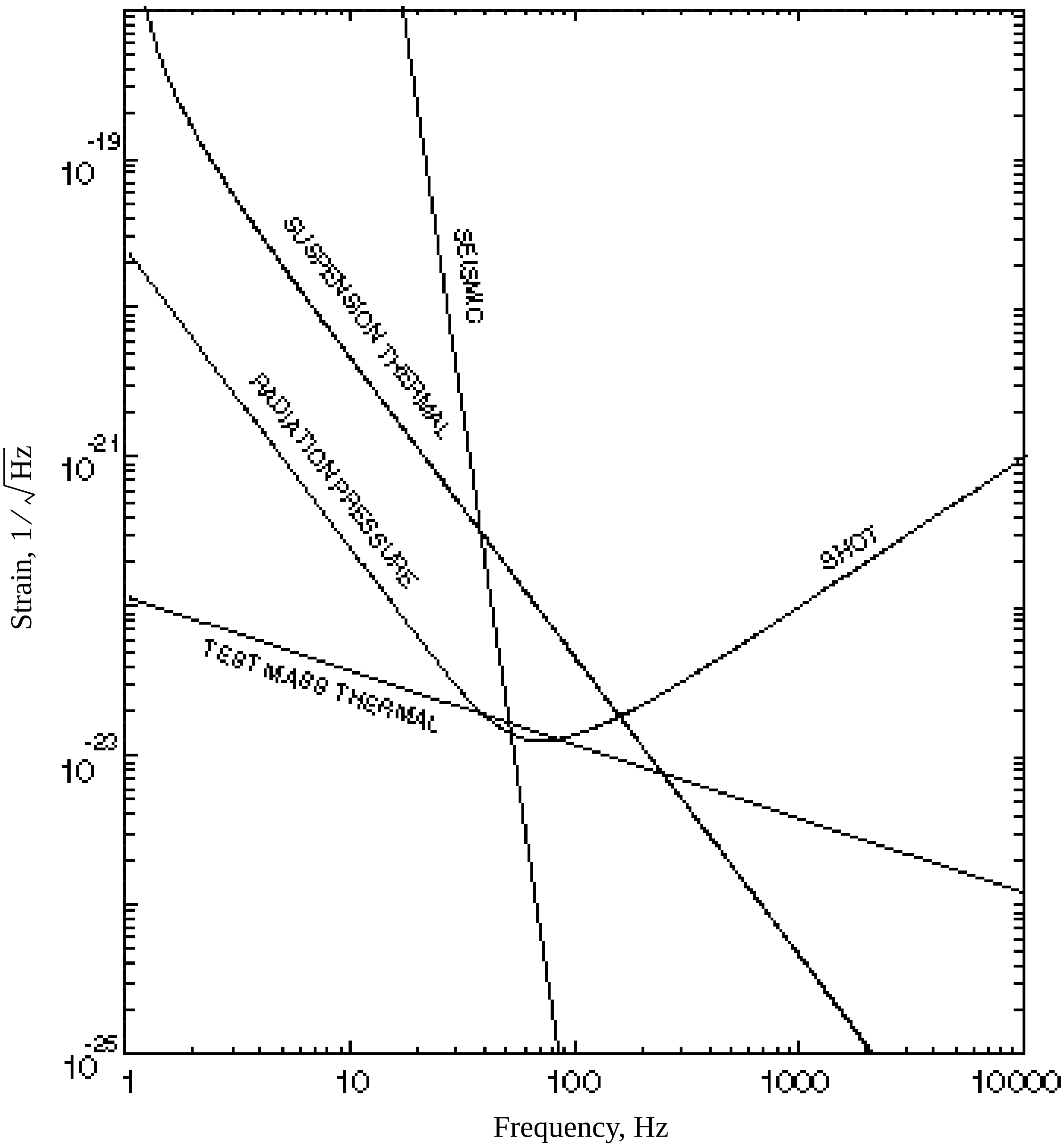

Figure 1: Initial LIGO interferometer sensitivity.

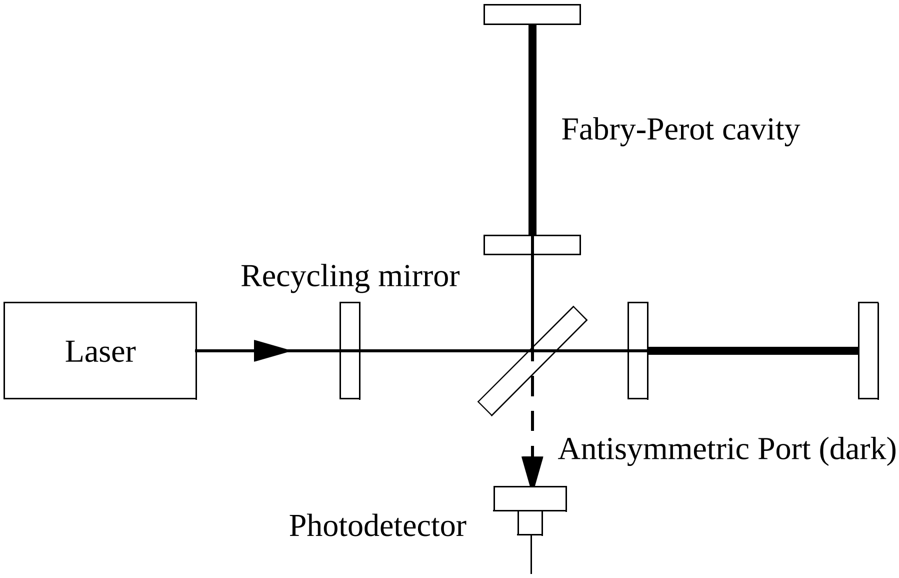

Figure 2: Power recycled interferometer with Fabry-Perot arm cavities.

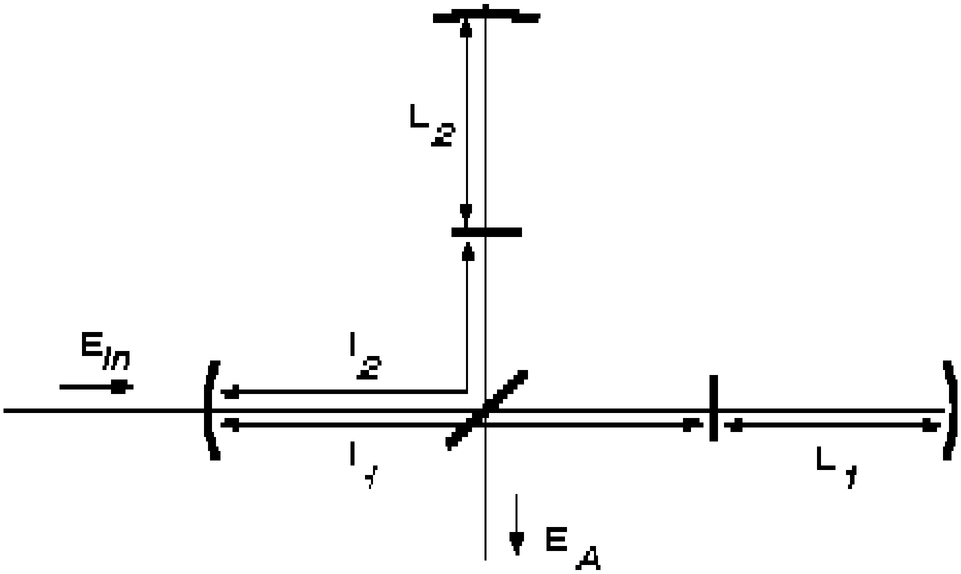

Figure 3: Asymmetric power recycled Michelson with Fabry-Perot cavities.

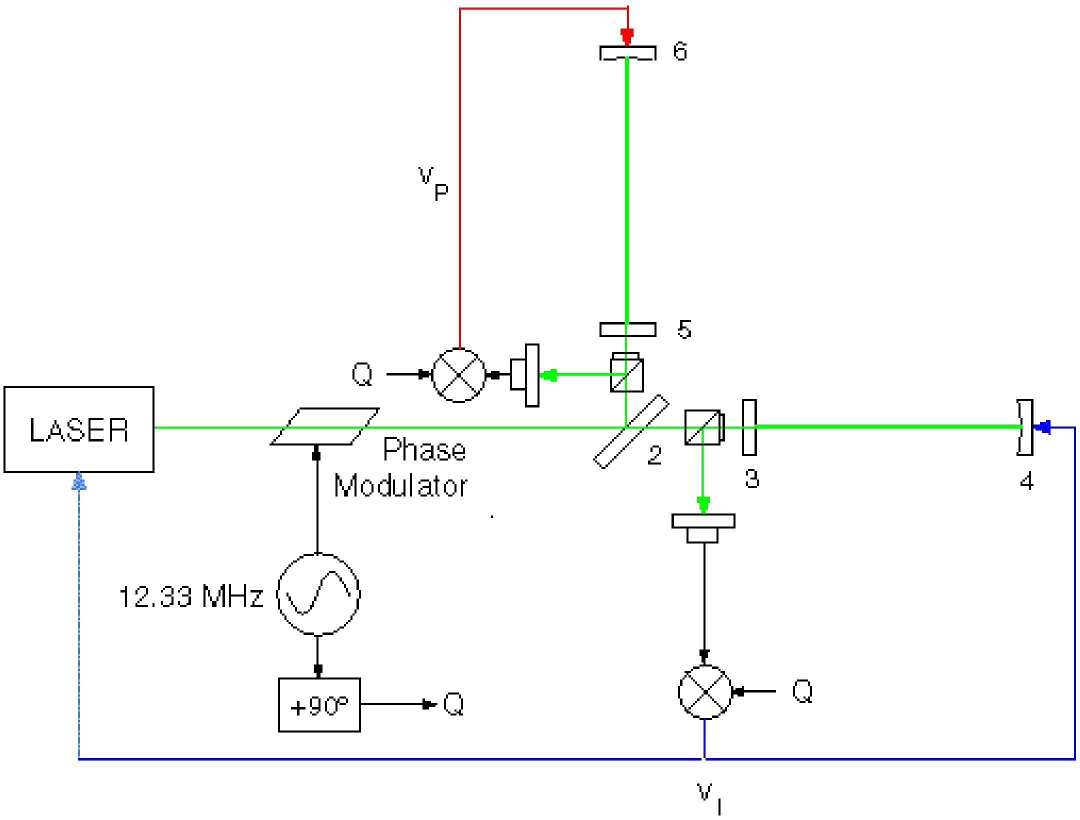

Figure 4: Fabry-Perot interferometer configuration.

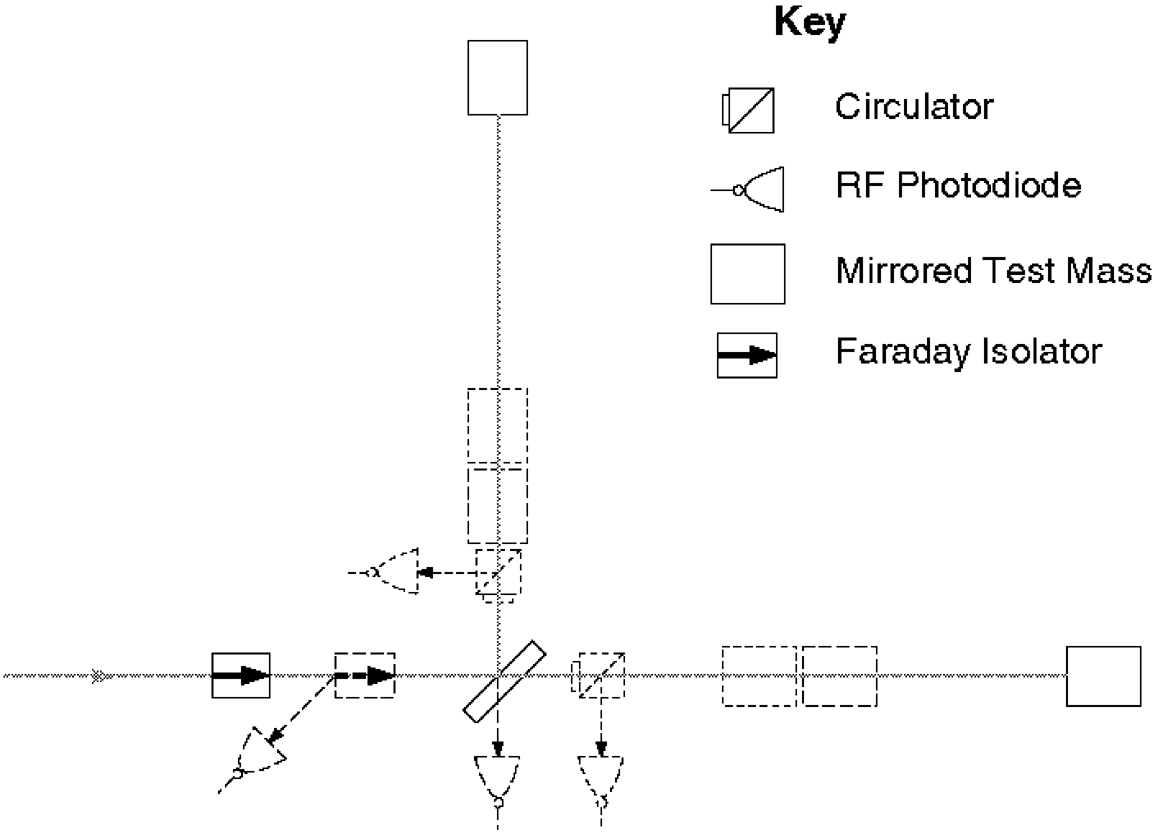

Figure 5: Physical modifications to the 40-m interferometer to change from a Fabry-Perot interferometer to recombined interferometer. Elements shown as dotted were moved or removed while the dashed elements show the new locations or elements that were added.

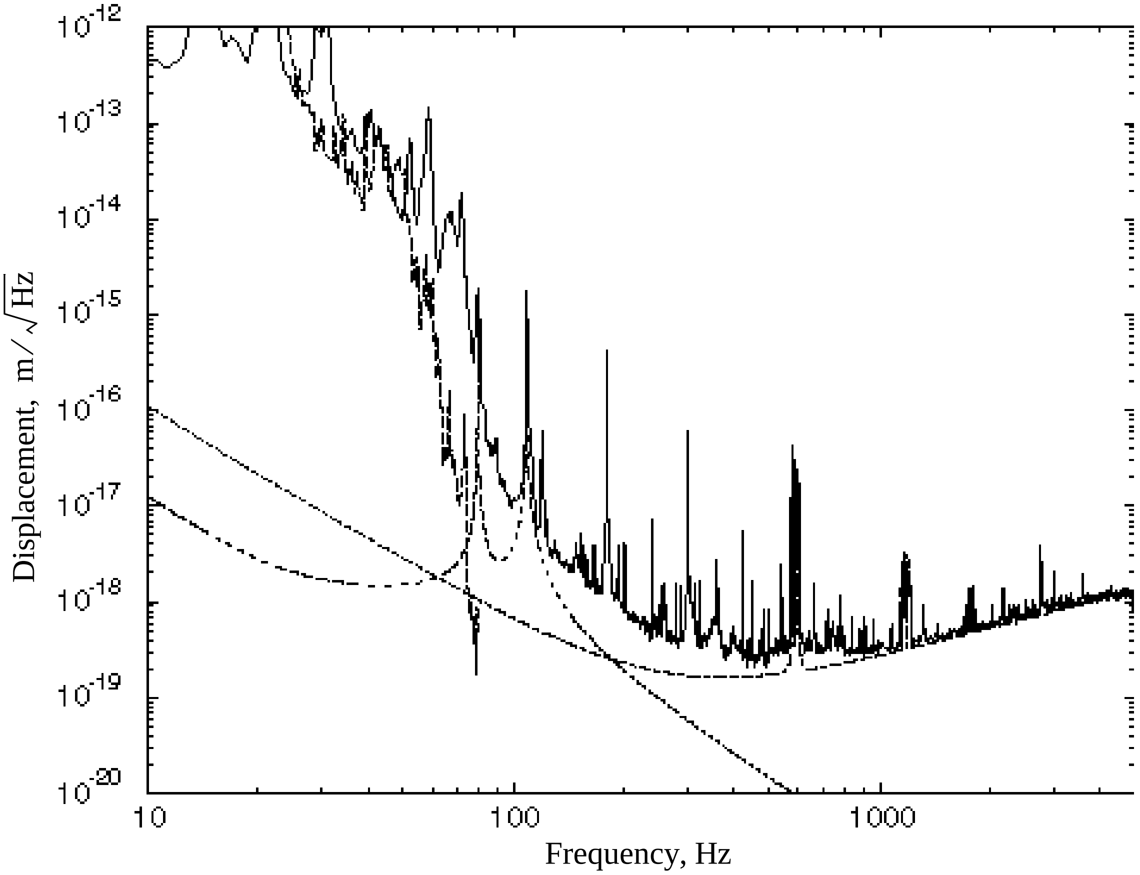

Figure 6: 40-m interferometer displacement noise spectrum on October 28, 1994, (solid) with estimated contribution from seismic noise (dashed), shot noise and thermal noise due to vibrations of the test mass and suspension wires (dot-dashed), and thermal noise in the test mass tilt resonances (dotted).

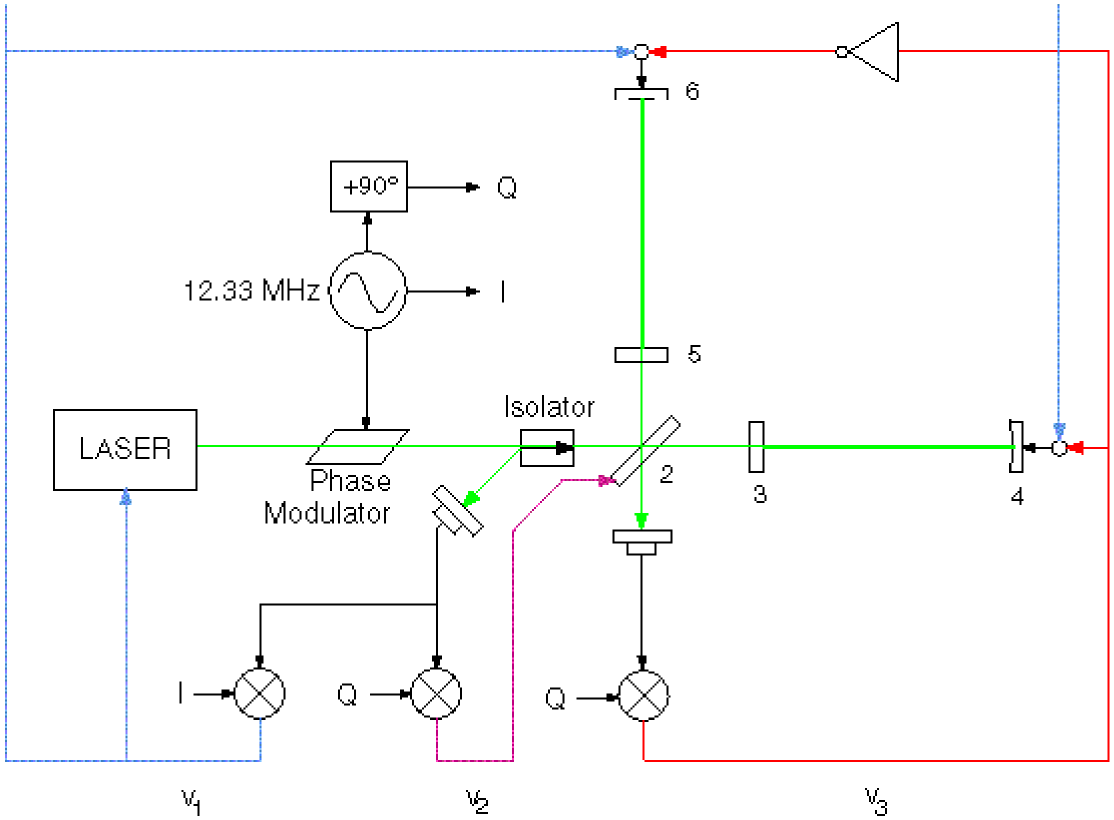

Figure 7: Recombined optical and servo topology.

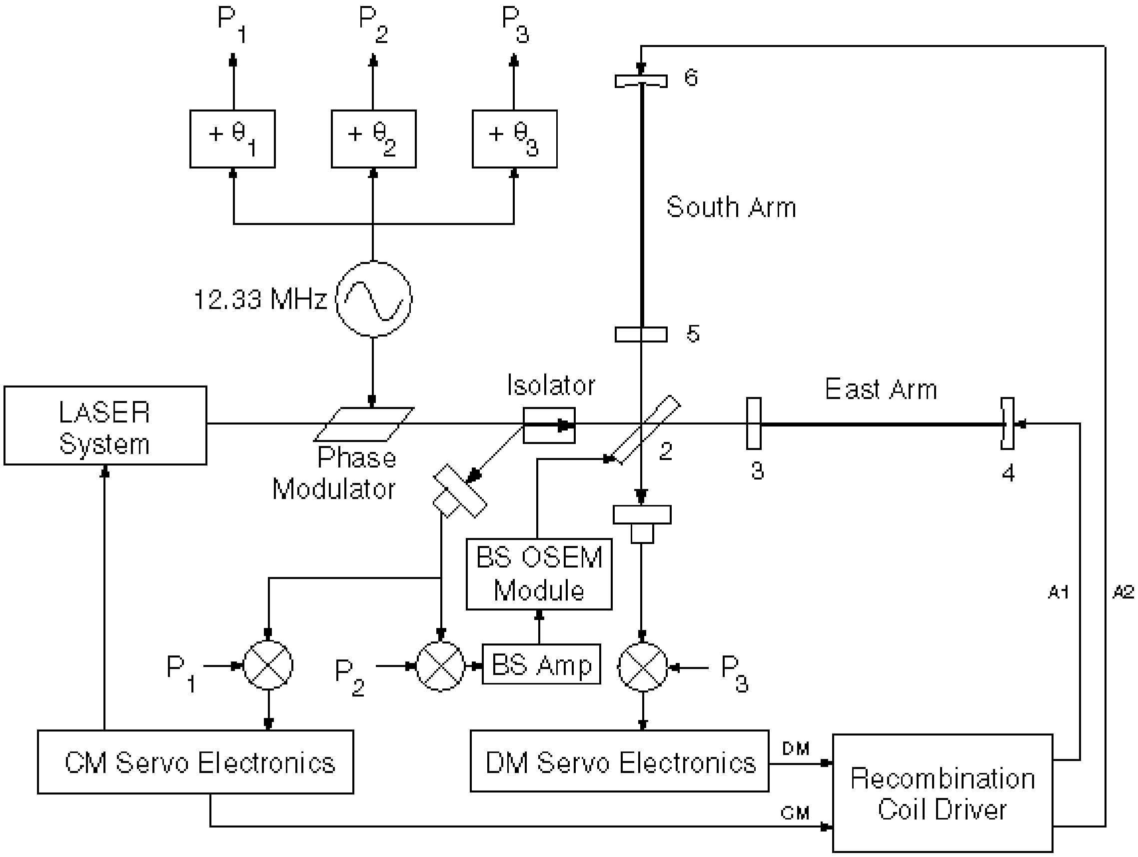

Figure 8: Block diagram of the length control servos for the recombined 40-m interferometer.

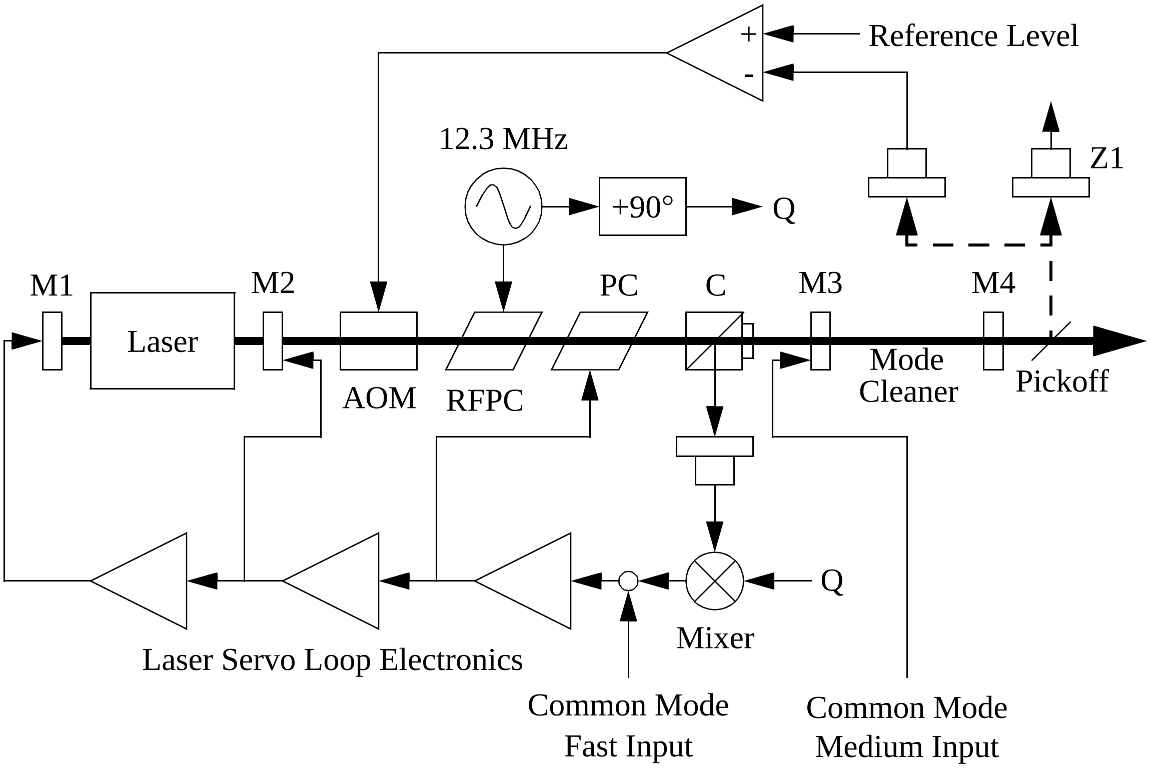

Figure 9: Laser frequency and intensity stabilization system. The laser frequency is changed by feeding back to the laser mirrors (M1 and M2) or phase correcting Pockel’s cells (PC). 12.3 MHz sidebands are put on the laser light with an RF Pockel’s cell (RFPC) and the light returning from the mode cleaner cavity (mirrors M3 and M4) is extracted with a circulator (C) for RF reflection locking.

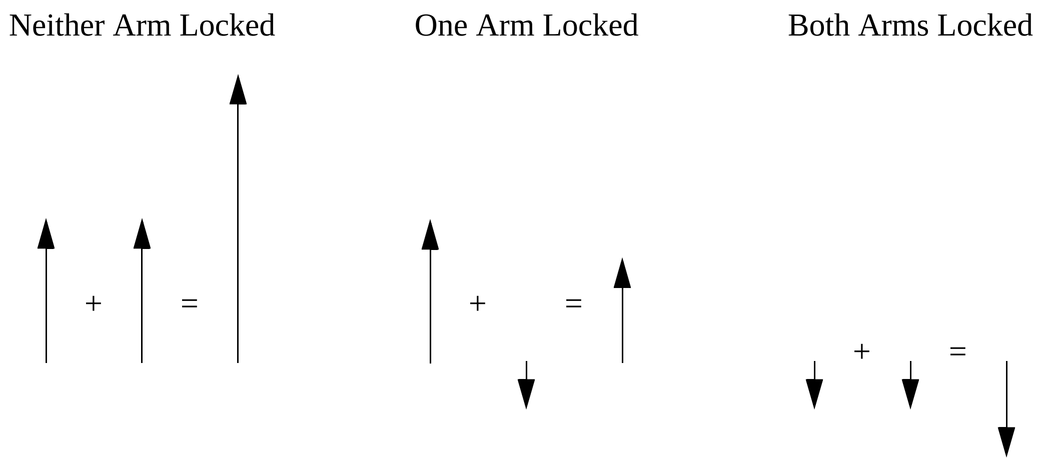

Figure 10: Phasor diagrams of light returning to the symmetric port. The two fields shown adding are the reflected carrier fields from the arm cavities and their sum is the field at the symmetric port.

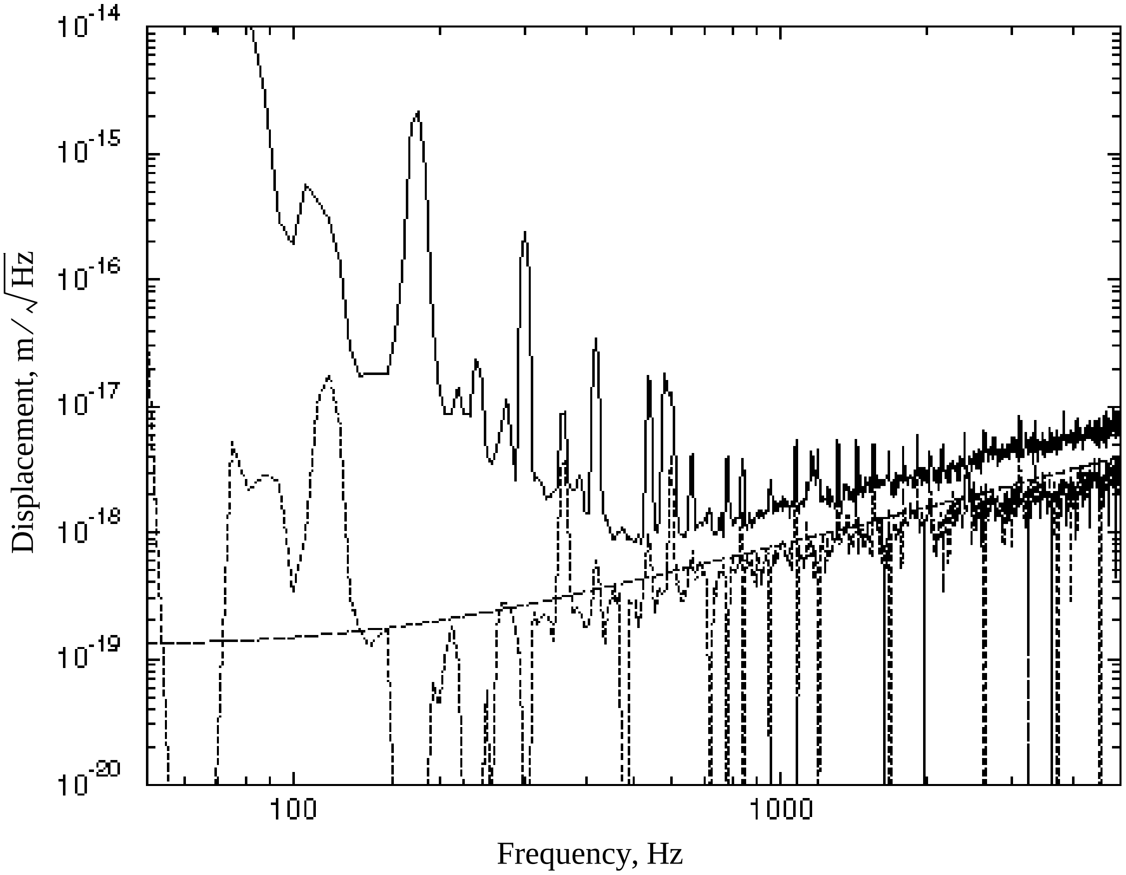

Figure 11: Calculated shot noise contribution to interferometer displacement spectrum (dashed), with empirical measurement of shot noise contribution (dotted) and interferometer displacement spectrum taken shortly before (solid).

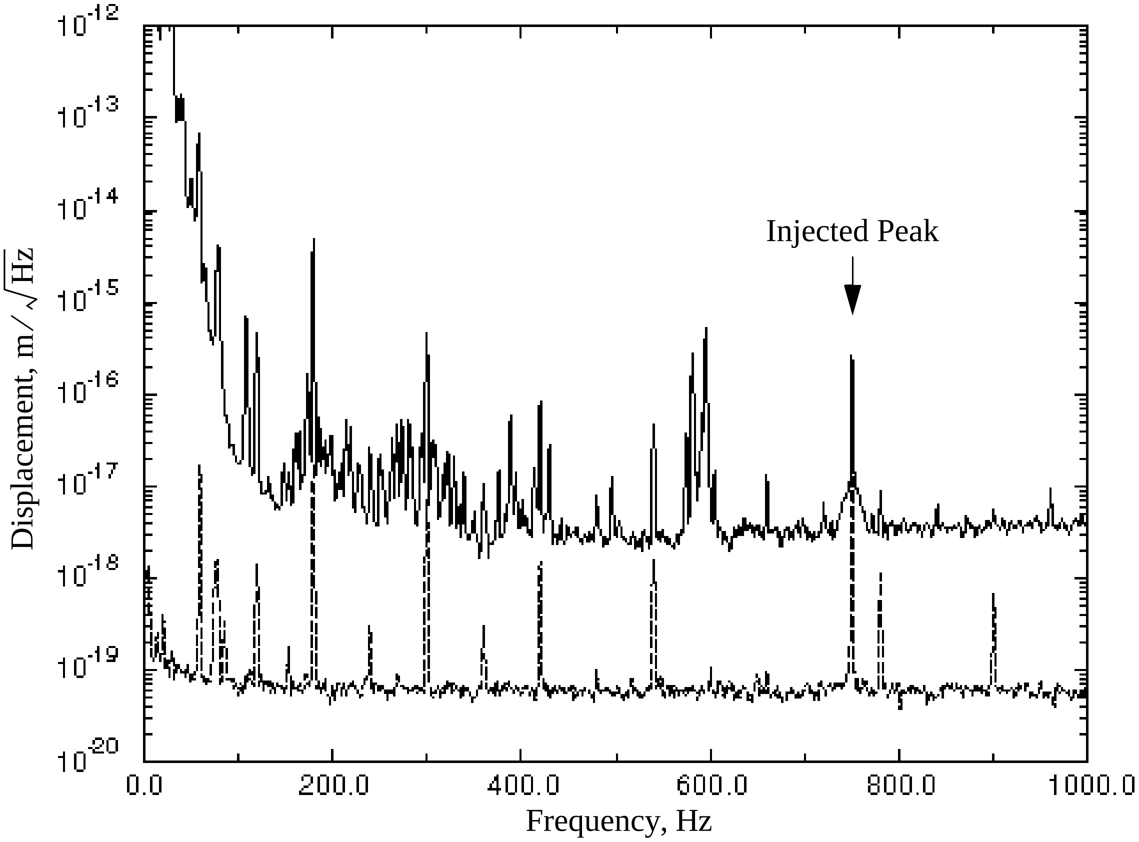

Figure 12: Estimated frequency noise contribution (dotted) valid only in a small region around the 750 Hz injected peak to the interferometer output (solid).

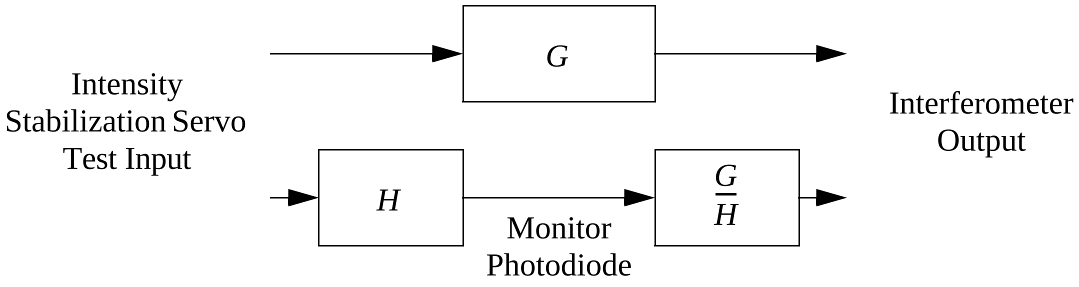

Figure 13: Transfer function method of measuring intensity noise contribution to interferometer output.

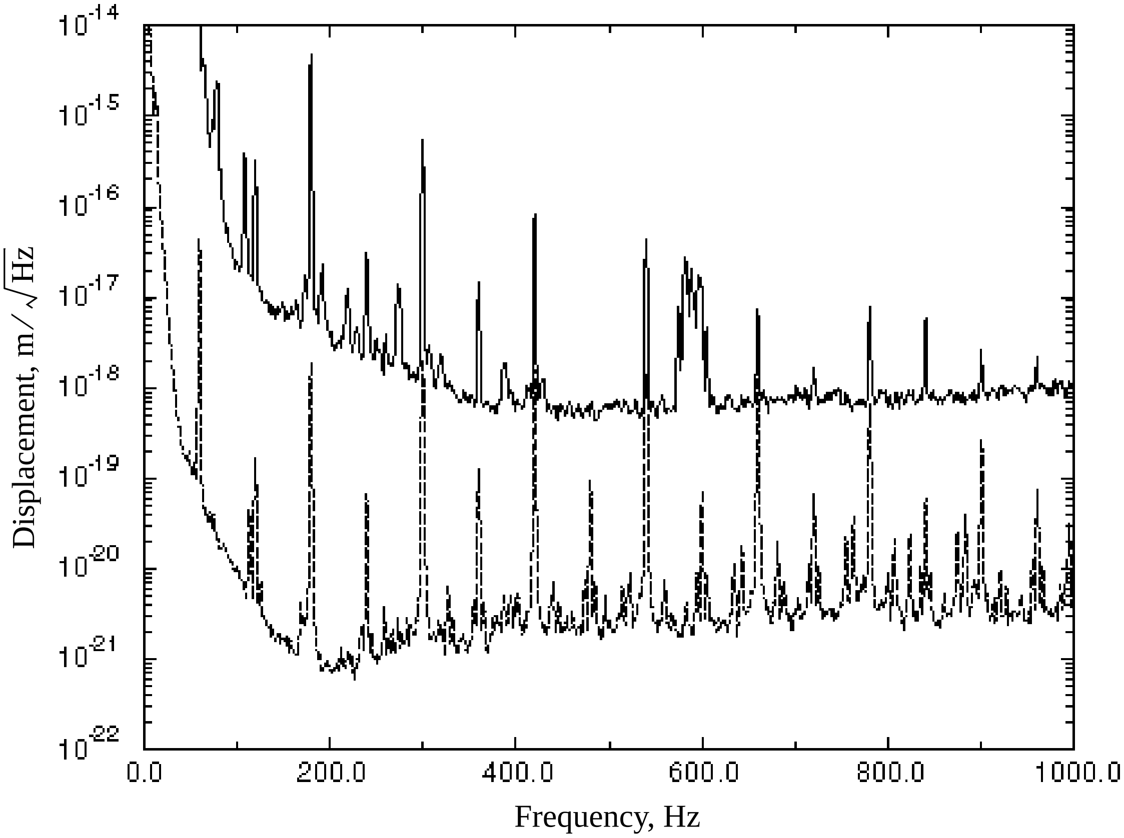

Figure 14: Estimated intensity noise contribution (dashed) to interferometer output (solid), using the transfer function method.

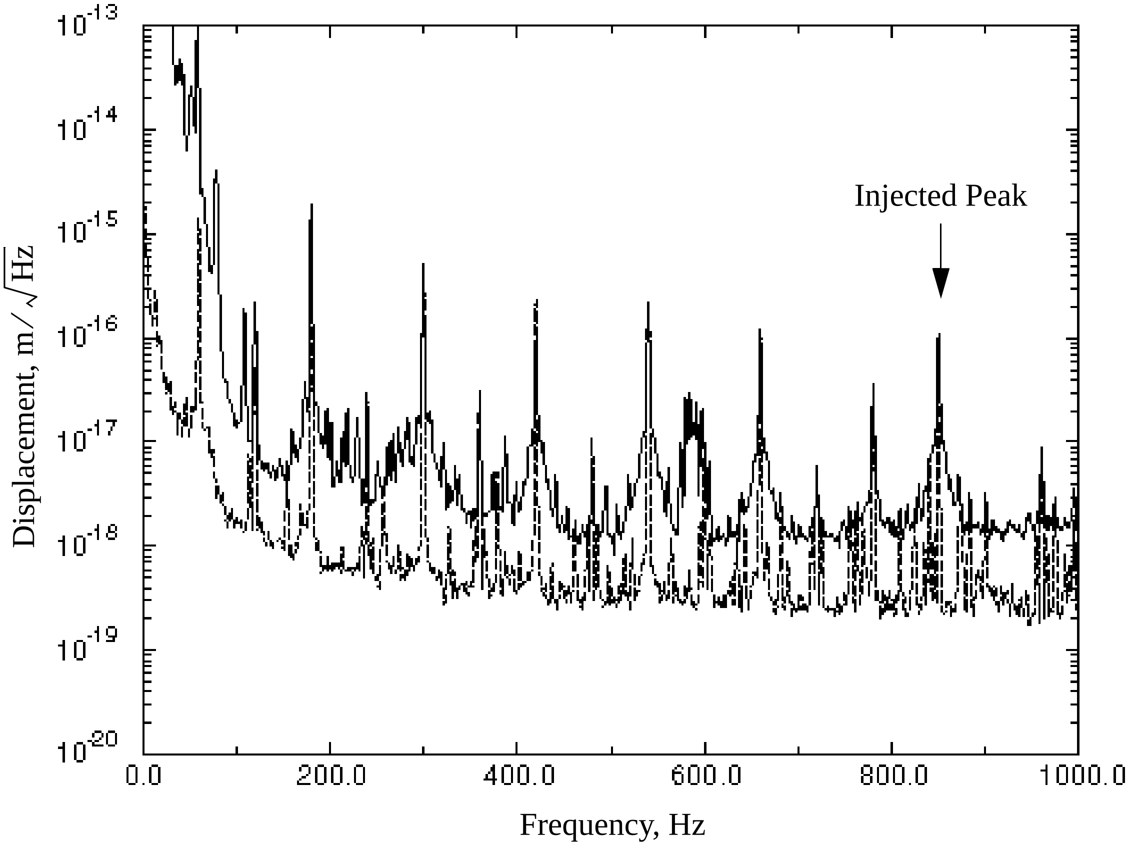

Figure 15: Estimated intensity noise contribution (dotted) valid only in a small region around the 850 Hz injected peak to the interferometer output (solid).

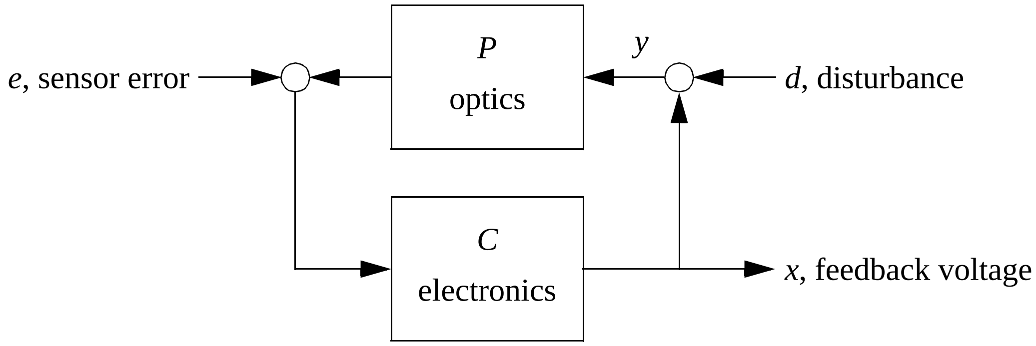

Figure 16: Diagram of beam splitter servo loop, showing various noise sources driving the beam splitter motion (*y*).

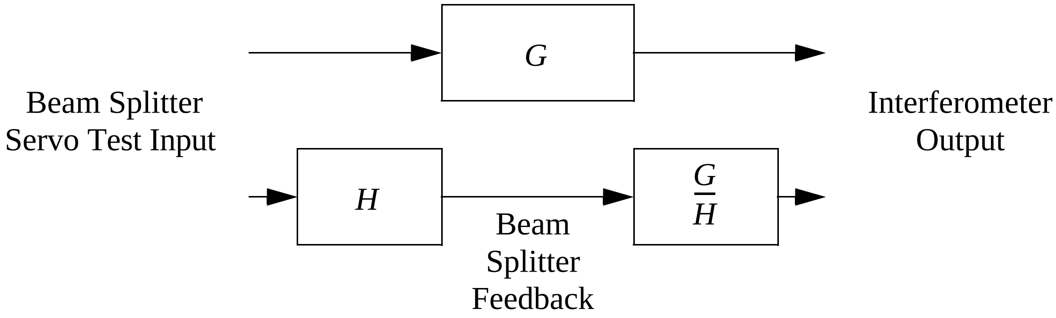

Figure 17: Transfer function method of measuring the beam splitter motion contribution to interferometer output.

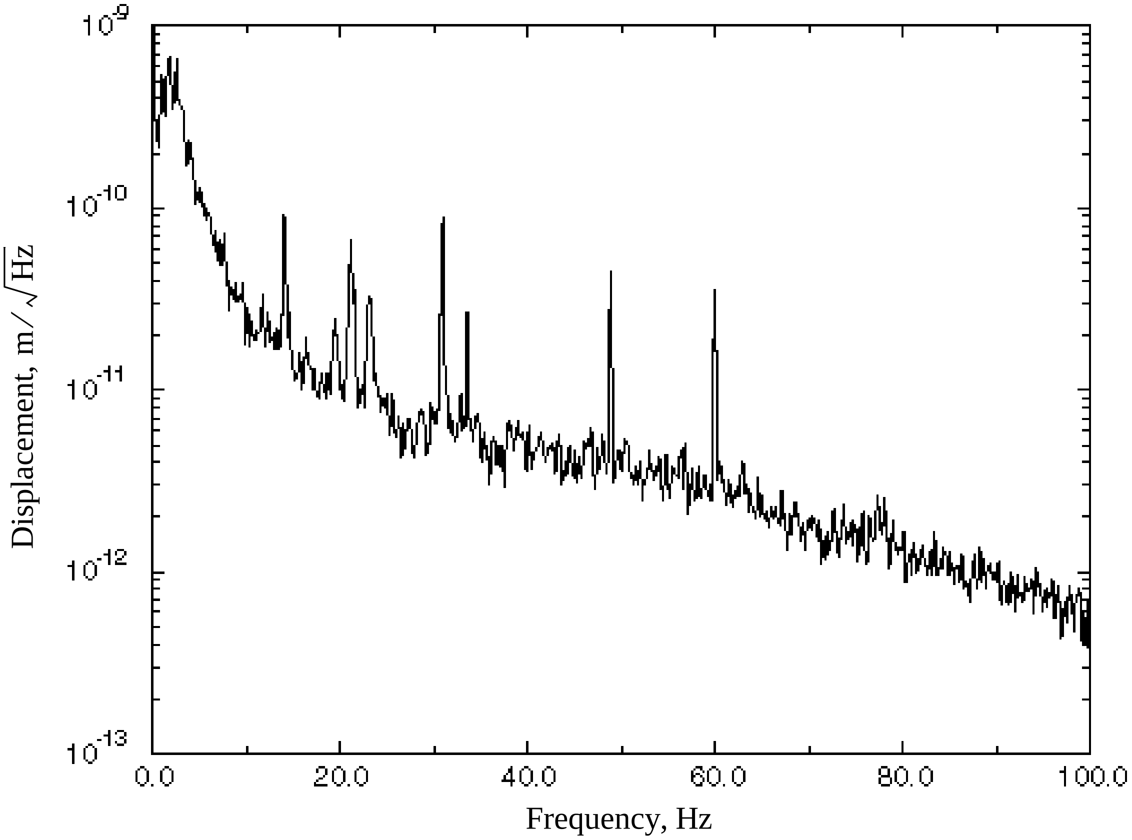

Figure 18: Residual beam splitter motion.

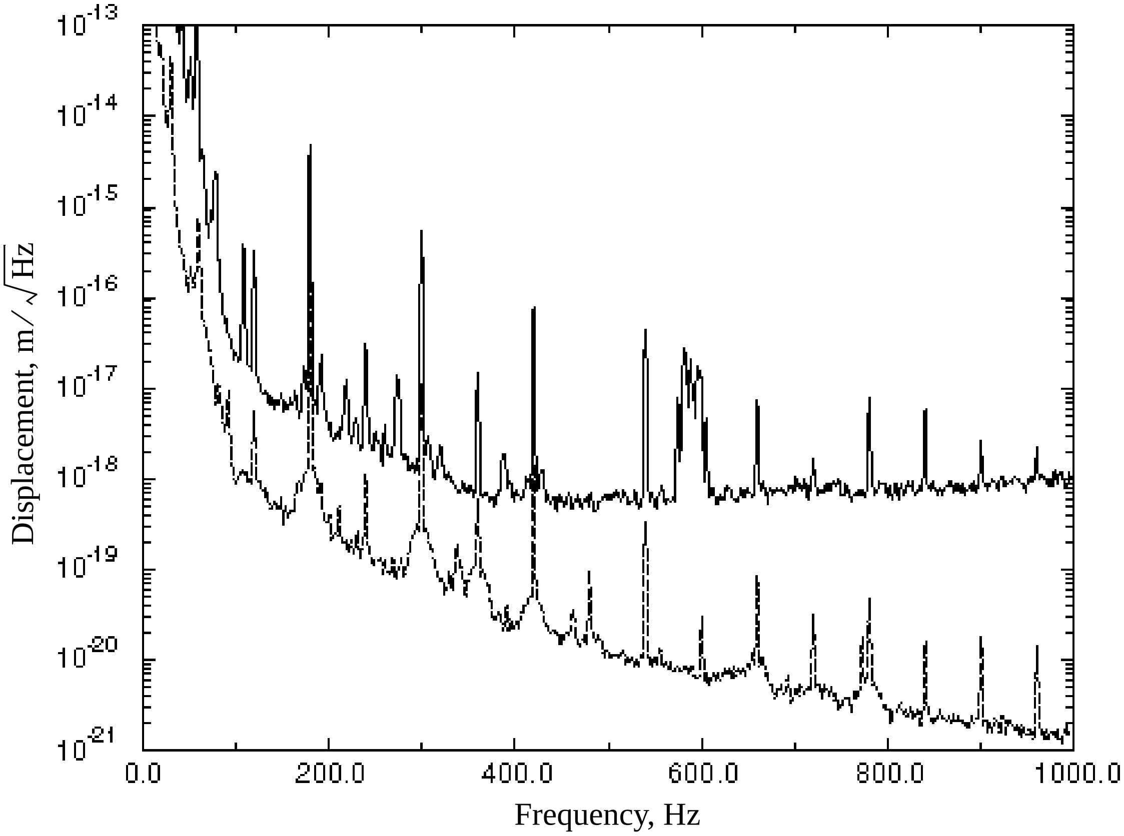

Figure 19: Beam splitter motion contribution to interferometer output (dotted) shown for comparison with the best interferometer noise spectrum (solid).

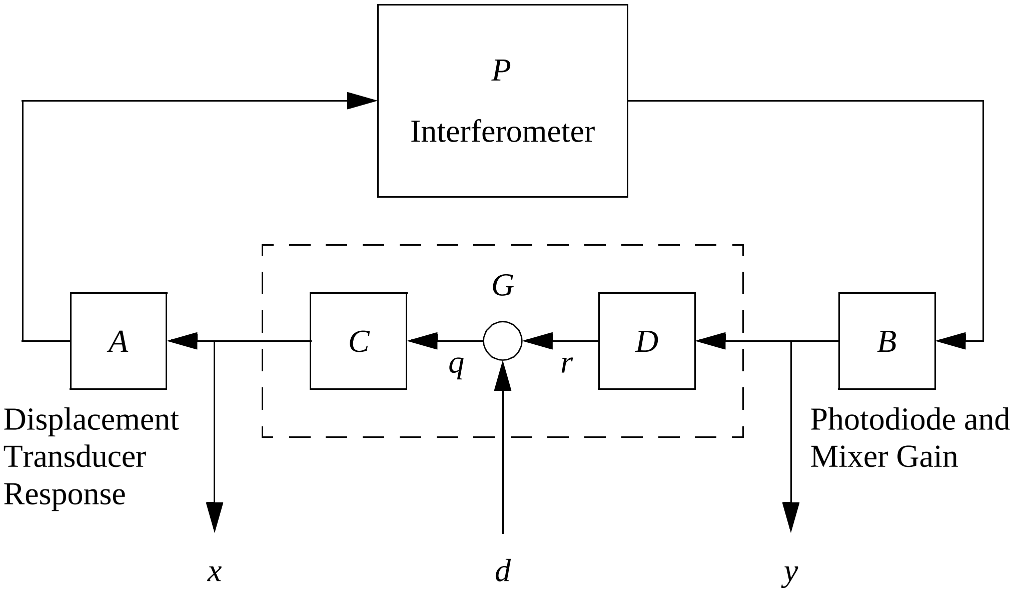

Figure 20: Block diagram of closed-loop interferometer showing signals extracted for interferometer response measurements.

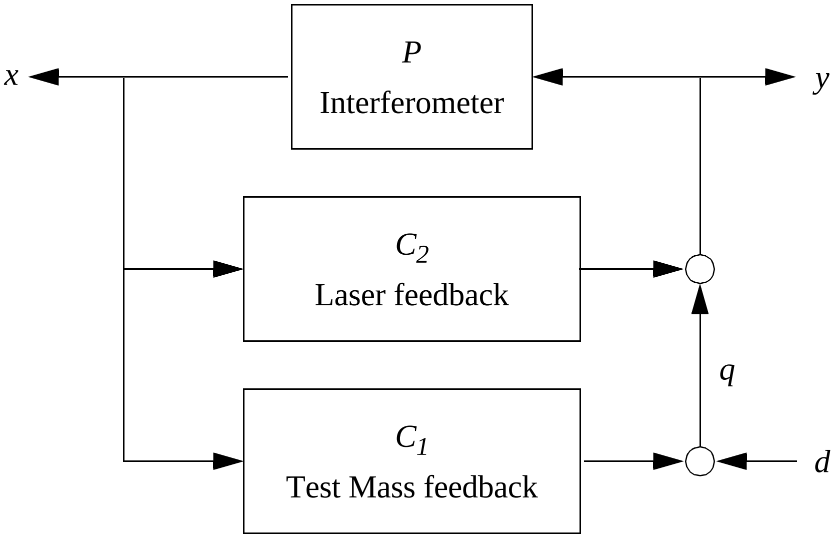

Figure 21: Simplified block diagram of common mode servo with two feedback paths.

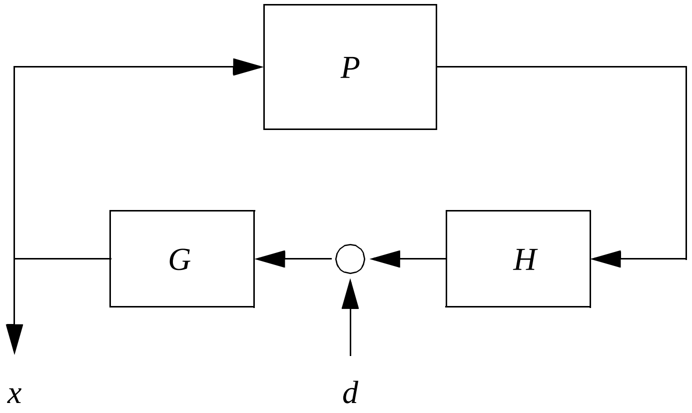

Figure 22: Block diagram of open loop gain measurement.